



Mapping Glacial Lakes in the Western Himalayas Using an Enhanced Breakpoint Method and CubeSat Imagery

Mustafa Javed^{1,2} · Jürgen Böhner³ · Shabeh ul Hasson¹

Received: 1 December 2023 / Accepted: 21 April 2025 / Published online: 27 June 2025
© The Author(s) 2025

Abstract

Glacier retreat leads to the formation of glacial lakes, which can become potentially dangerous for outburst flooding, posing a serious risk to the lives and infrastructure of mountainous communities. To better manage such risk, frequent mapping and precise monitoring of glacial lakes are essential yet hindered by inaccessible terrain, severe climatic conditions for in-situ measurements, or a tedious manual mapping of coarse-resolution satellite imagery. Here, we propose an enhanced breakpoint method (EBM) that adopts for each lake an individual histogram prepared by applying a dynamical buffer around that lake. We employ EBM to develop the glacial lake inventories for the Astore Basin within the western Himalayas for 2018 and 2019 using ultra-high resolution (~3 m) optical PlanetScope imagery. Our semi-automated EBM outperforms similar methods and precisely maps glacial lakes of all sizes and complexities with little manual mapping and editing using high-resolution imagery from PlanetScope as well as coarser resolution imagery from Sentinel-2 and Landsat-8 platforms. Intercomparison of 2018 and 2019 inventories and the existing 2013 inventory revealed heterogeneous lake formations, disappearances, expansions, and shrinkage patterns. In 2013, 196 lakes had a total area of 5.847 km² and a corresponding volume of 0.073 km³. By 2018, 135 lakes formed newly, whereas 9 lakes drained out, leading to an overall increase in the number of lakes by 64.28% (196) to 322 lakes. Over the five years of 2013–2018, 40 lakes expanded, whereas 147 lakes shrank, resulting in an overall reduction in area by –1.50% to 5.759 km² and a decrease in volume by –5.56% to 0.069 km³. As compared to 2018, 213 lakes expanded, whereas 98 lakes shrank, experiencing an overall area expansion of 3.83% to 5.98 km² and an increase in volume by 4.65% to 0.072 km³. These findings suggest that changes for 2018–2019 are higher than that of the 2013–2018 period. Employing daily PlanetScope imagery at ~3 m resolution, the EBM can precisely map and monitor lake evolutions with low latency time to reduce and mitigate outburst flooding risks in complex terrain.

Keywords Glacier retreat · Glacial Lakes · PlanetScope imagery · Astore · Himalayas

1 Introduction

Lakes are vital ecological assets that provide a lifeline to the aquatic and terrestrial ecosystems. More than 100 million lakes existing on Earth at present collectively hold around 87% of the Earth's freshwater resources and play a critical part in the local to global water cycle (Verpoorter et al.

2014; Yao et al. 2023). Lakes present in glaciated environments exhibit a history of glacial and climatic activities within their catchments (Miehe et al. 2021). The role of serving as a proxy to local and regional changes in the drainage basin makes these lakes further suitable for investigating the terrestrial response to present and paleoclimatic changes (Adrian et al. 2009). Global warming induced vanishing of snowpacks and permafrost, thinning, and retreat of glaciers, intensified melting, and extreme flood and drought events lead to the formation and disappearance of lakes as well as their expansion and shrinkage (Zhao et al. 2018; Wang et al. 2013). Such dynamics are supposedly more visible within High Asia, featuring complex terrain, harsh environments, and being earlier victims of adverse climatic changes (Pepin et al. 2015; Bolch et al. 2019). In recent decades, the number of glacial lakes has increased by 50% worldwide and by 9% within the Himalayas (Shugar et al.

✉ Shabeh ul Hasson
shabeh.hasson@uni-hamburg.de

¹ HAREME Lab, Institute of Geography, CEN, Universität Hamburg, Hamburg, Germany

² Research Department II: Climate Resilience, Potsdam Institute for Climate Impact Research, Potsdam, Germany

³ Institute of Geography, CEN, Universität Hamburg, Hamburg, Germany

2020; Nie et al. 2017). Further, the Himalayan lakes have seen an area expansion of 14% over the 1990–2015 period (Nie et al. 2017).

Depending upon the geomorphology of lakes and the hydro-climatic conditions of their catchment, these highly dynamic water bodies can become potentially dangerous for the outburst flooding, known as the Glacier Lake Outburst Flood (GLOF) (Zhang et al. 2015). Under prevailing climatic changes, the observed amplified occurrence of snow/ice avalanches and landslides accompanied by shifts in the environmental stability and the subsequent burgeoning expansion and formation of glacial lakes have substantially augmented the likelihood of GLOF events (Worni et al. 2013; Ding et al. 2021; Yao et al. 2019). For instance, more than 100 GLOF events have been reported within the Himalayas since the 1900s (Nie et al. 2018; Zheng et al. 2021a; Zhang et al. 2022), while their frequency exhibits a rising trend (Harrison et al. 2018; Yao et al. 2014; Zheng et al. 2021b). On the other hand, there is no long-term trend observed in the frequency of GLOFs, despite distinct trends in the number and area of lakes (Hock et al. 2019; Veh et al. 2019).

Regardless of the triggering mechanism, an abrupt release of massive water volume leads to the inundation of large surrounding and downstream areas with no lead time to manage the disaster. Hence, reducing or mitigating the GLOF risk needs early monitoring of all lakes to assess their transition between becoming potentially dangerous and vice versa. The first step towards such monitoring involves mapping the evolution (formation, disappearance, expansion, and shrinkage) of lakes (Bajracharya and Mool 2009). Therefore, the generation of a precise and updated glacial lake inventory is the starting point in analyzing the potential GLOF hazards within High Asia (Worni et al. 2013; Ives et al. 2010; Bhambri et al. 2018; Mal et al. 2020). However, there is a gap in the accurate delineation of glacial lake shorelines using high-resolution CubeSat imagery. Furthermore, our understanding of the location and mobility of glacial lake shorelines is still insufficient regarding their formation and development. To minimize damage related to GLOFs, a better understanding of lake shoreline dynamics is required. An updated and precise glacial lake inventory is essential for assessing hazard risk, understanding the dynamics of associated glaciers, and comprehending the lakes' spatiotemporal distribution. As such, the Astore Basin's glacial lake inventory needs to be updated, and its boundaries are precisely mapped.

Several studies have developed lake inventories within High mountain Asia at local and regional scales (Das et al. 2024; Ahmed et al. 2022; Gupta et al. 2022; Li et al. 2022; Furian et al. 2021; Chen et al. 2020; Wang et al. 2020; Zhang et al. 2021). Specifically, Landsat datasets are being widely used to map glacial lakes owing to their extensive

spatial coverage, long span of record, and easy accessibility (Khadka et al. 2018; Nie et al. 2017; Shrestha et al. 2017). Studies either applied binary classification (Roach et al. 2012; Plug et al. 2008) or fractional mapping of pixels to segment an image into water and non-water pixels (Ji et al. 2008; Rover et al. 2010). Binary glacial lake mapping, based either on an automated or semi-automated approach, has been performed using different spectral band ratio combinations, NDWI thresholding, global-local segmentation, object-oriented classification, and the decision tree approach (Gardelle et al. 2011; Li et al. 2011; Nie et al. 2017; Veh et al. 2018). Whereas water bodies have been mapped for the coarse-resolution imagery of AVHRR (Klein et al. 2014; Dietz et al. 2017) and MODIS (Sun et al. 2011; Weiss and Crabtree 2011) by applying the spectral unmixing technique to enhance the accuracy.

Here, we develop a semi-automated methodology to precisely delineate glacial lake shorelines for the western Himalayan basin of Astore using high spatiotemporal resolution CubeSat imagery (PlanetScope) for the years 2018 and 2019. Due to automation, this methodology will expedite the mapping process in the first place. Additionally, the high-resolution imagery will enhance precision. To accomplish this objective, we have improved a water classification approach of the Enhanced Breakpoint Method (Olthof et al. 2015) that employs dynamic buffering. The methodology was validated against manually delineated glacial lakes and compared to the existing regional inventory of Wang et al. (2020). We further assessed the sensitivity of our developed methodology to the selection of parameters and to the coarse spatial resolution of Landsat-8 and Sentinel-2 imagery. The glacial lake changes were quantified in terms of number, area, depth, and volume. Finally, we discussed a few limitations of optical imagery in delineating the lake shorelines within complex Himalayan terrain.

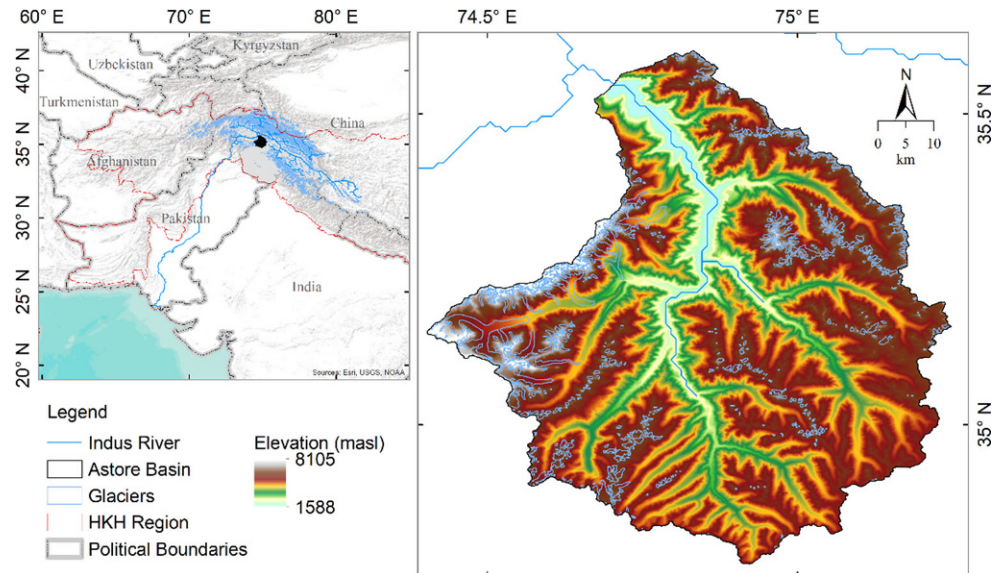
2 Materials and Methods

2.1 Study Area

Under the rain shadow of the western Himalayas, the Astore basin is situated between 34.77° and 35.64° North and 74.41° and 75.24° East (Fig. 1). The Astore River originates from the west of Burzil Pass, drains the Deosai plateau in the northwestward direction, and joins the main trunk of the Indus River downstream of its confluence with the Shyok and Shigar tributaries. Featuring a complex terrain, the basin spans over 3990 km² of surface area with a mean elevation of 4100 m and an elevation range of 1500–8000 m (Hayat et al. 2019).

The climate of the region is influenced by both the south Asian summer monsoon and the western disturbances.

Fig. 1 Astore Basin topography, river network, and High Asia extents



Three meteorological stations within the basin, namely Astore, Rattu, and Rama, suggest that the minimum and maximum monthly average temperatures are observed in January (-1.9°C) and August (20.7°C), respectively (Hayat et al. 2019). The hydrology of the basin is mainly fed by the melting of snow, which is received under the precipitation regime associated with the westerly disturbances during winter and spring (Hasson 2016; Hasson et al. 2017). Around two-thirds of the annual total precipitation falls during winter and spring (Hayat et al. 2019). The south-westerly moist flow during the summer monsoon months of July–September is largely blocked by the western Himalayas, although offshoots can approach the basin (Ali et al. 2009).

Mean snow cover ranges between $2 \pm 1\%$ and $98 \pm 1\%$ of the basin area within a year (Hasson et al. 2014) whereas only $\sim 6\%$ (248 km^2) of the basin area is engulfed by glaciers, which possibly contributes a minute amount of meltwater to the overall discharges (Tahir et al. 2016). Based on hydrological regime analysis, Hasson et al. (2017) designated the Astore basin as mainly the snow-fed basin. The Astore River drains around 3.45 million acre-feet (MAF) of water, contributing approximately 4.6% of the total discharge volume of the Indus River at the Tarbela reservoir (Ahmad et al. 2018). The basin hosts mainly the erosion lakes, which indicates its past glaciation.

2.2 Optical Imagery and Auxiliary Dataset

We obtained optical imagery from PlanetScope (PS), Sentinel-2 (S2), and Landsat-8 (L8) sensors for clear-sky days centered around September 01, 2018, and 2019, covering the entire Astore Basin. Mapping was mainly performed using PS imagery, whereas S2 and L8 data

were used to analyze the sensitivity of our method across multiple and coarse-resolution sensor imagery.

PlanetScope: PS imagery is based on a Planet Lab's constellation of 180+ small optical imaging framing camera platforms, called doves, which have been observing the Earth's surface daily at $\sim 3\text{-meter}$ spatial resolution. We obtained a Planet Level 3A data product (Analytic Ortho Tile Product), available at a 3.125 m resolution under the education and research program of Planet Labs (<https://www.planet.com/explorer/>).

Sentinel-2: A constellation of twin polar-orbiting satellite platforms known as Sentinel-2A and Sentinel-2B is a multi-spectral imaging mission with a Multispectral Instrument (MSI) sensor, which acquires optical imagery at a medium spatial resolution of 10 to 60 m and temporal resolution of five days when combined, or 10 days individually. The Sentinel-2 scenes processed for this study were downloaded from <https://earthexplorer.usgs.gov/>.

Landsat-8: Landsat-8 Operational Land Imager (OLI) has radiometric precision over a 12-bit dynamic range and a positional accuracy above 12 m. The spatial resolution of Landsat-8 is 30 m for multispectral, 15 m for panchromatic, and 100 m for thermal bands. The temporal resolution of Landsat-8 OLI is 16 days. We obtained the Terrain Precision Landsat-8 scenes of Collection 1, Tier 1 from the Earth Explorer at <https://earthexplorer.usgs.gov/>.

Shuttle Radar Topography Mission (SRTM): This dataset offers high-resolution elevation data of the Earth's surface with global coverage at a spatial resolution of 30 meters (1 arc second), derived from spaceborne radar. The Earth Explorer platform from the United States Geological Survey (<https://earthexplorer.usgs.gov/>) allows users to search, visualize, and download SRTM data.

2.3 Methodology

After acquiring the required dataset, first, we performed the sensitivity analysis to assess whether the lake mapping technique is sensitive to the choice of parameter values and which parameters are the most sensitive. After the sensitivity analysis, we mapped the lakes using PS imagery obtained for September using an enhanced version of the breakpoint method (EBM). The breakpoint method maps the area of each lake by determining the thresholds for pure water pixels and surrounding land pixels based on a single NDWI bimodal histogram prepared for the whole image based on all lake areas with constant (CBI) buffers applied. We enhanced the breakpoint method in two ways: 1) to use a single NDWI bimodal histogram for the whole image based on all lake areas with dynamic buffers instead of constant buffers (DBI), and 2) to use an individual NDWI bimodal histogram prepared for each lake with dynamic buffer applied around that lake (DBL). We designated DBL as EBM.

To check the robustness of our semi-automated methodology, we validated the EBM by comparing the semi-automatically mapped lake areas using clear sky PS imagery of 01 September 2018 against the 38 reference lakes of different sizes and complexity mapped manually on the same PS imagery. Then, over a large area, we additionally assessed whether three methods can be applied to coarse or medium-resolution satellite imagery across platforms (PS, Sentinel-2, and Landsat-8) and whether the EBM outperforms similar breakpoint methods against a reference dataset of 22 lakes mapped manually using PS imagery. To assess the added value of local scale precise mapping using high-resolution imagery, we further compared the EBM methodology with a regional-scale inventory developed by Wang et al. (2020) for the same year 2018 using Landsat imagery.

Based on validated methodology, we prepared lake inventories for the years 2018 and 2019. We compared the lake evolution during 2013 and 2018 by comparing the lake inventory of 2018 with an existing inventory of 2013, manually prepared by the Pakistan Meteorological Department (PMD) using the Landsat imagery. We also assess how lakes evolved between 2018 and 2019. After mapping the glacial lakes, we estimated lake volumes and mean depths using empirical relationships (**Supplementary Table 2**).

2.3.1 Sensitivity Analysis of Lake Mapping

We assess whether the lake mapping technique is sensitive to the choice of parameter values and which parameters are the most sensitive. These include a global NDWI threshold that identifies initial lake locations, a hillshade threshold that reduces shadow effects, and a parameter, C ,

that finally decides on the thresholds of 100% land and 100% water pixels. Sensitivity to the global NDWI and hillshade thresholds has been assessed by manually applying varying thresholds on a list of random NDWI rasters from the analyzed archive and inspecting their results against the reference datasets. The objective is to determine the safest thresholds that work in all situations, although imperfectly, and in an automated fashion. Whereas for C , a reference lake centered at 74.65°E 34.91°N featuring an area of 6560 m² was mapped in a semi-automated process with nine values of C ranging between 0.55 and 0.95 with an increment of 0.05, and the calculated lake area was then compared against the manually delineated area to determine the best threshold. We further assessed whether changes in the estimated lake area occurred due to varying C are compensated by the water fraction percentages (100%, $\geq 75%$, $\geq 50%$, $\geq 25%$, $\geq 10%$, and $>0%$) considered for calculating the total lake area.

2.3.2 Validation Across Platforms

To validate our methodology, we compared the semi-automatically mapped lake areas against the 38 reference lakes of different sizes and complexities mapped manually on the same clear sky PS imagery of 01 September 2018. This validation was performed for the lake areas calculated based on all considered water fractions (100%, $\geq 75%$, $\geq 50%$, $\geq 25%$, $\geq 10%$, and $>0%$) to identify which water fraction should be considered for calculating lake areas. To quantify inter-dataset differences, we employ the statistical measures of mean bias in percentage (PBIAS), coefficient of determination (R^2), root mean square error (RMSE), and normalized RMSE (nRMSE). The lower values of PBIAS, RMSE, and nRMSE and higher values of R^2 indicate better inter-dataset agreement.

On successful validation, we further assessed whether our methodology can be applied to coarse or medium-resolution satellite imagery. For this purpose, 22 lakes of different sizes and complexities were delineated semi-automatically from the Landsat-8 OLI (30 m), the Sentinel-2 MSI (10 m), and PS (~3 m) imagery dated 24 September 2019, 10 September 2019, and 10–13 September 2019, respectively, and the estimated lake areas were compared to manually delineated lake areas from PS imagery.

Using the same imagery from PS, Landsat-8, and Sentinel-2, we additionally showed how our method for lake area estimation based on the individual NDWI histograms generated from a Dynamical Buffer around each individual Lake (DBL) yields better results relative to similar methods. For this, we compared DBL to a single histogram either generated from Dynamically Buffered lakes of the whole Image (DBI) or Constant Buffered lakes of the whole Image (CBI), irrespective of the lake

size, type, and complexity. We compared these approaches, particularly for the PS imagery, but additionally for the Sentinel-2 and Landsat-8 imagery. In the case of CBI, we applied a constant buffer of 60m around all potential lake polygons within the image, as suggested by Cooley et al. (2017), and calculated the thresholds and subsequent lake areas on a single bimodal NDWI histogram for all buffered lake polygons. In the case of DBI, we instead applied a dynamical or varying buffer to each potential lake polygon in the image but again calculated the thresholds and subsequent lake areas based on a single bimodal NDWI histogram for all buffered lake polygons.

We further compare the developed inventory with the regional lake inventory developed by Wang et al. (2020) for the same year of 2018 using Landsat imagery, to assess the added value of local scale precise mapping using high-resolution imagery.

2.3.3 Lake Area Mapping

The extraction of inland water bodies from satellite imagery is non-trivial, particularly within the complex Himalayan terrain, where cloud confusion, lake freezing, soil saturation, and mountain shadows hinder precise mapping. Our semi-automated methodology addressed these issues in dedicated steps (Fig. 2). First, we calculated the Normalized Difference Water Index (NDWI) (McFeeters 1996) to enhance the water pixels and suppress the vegetated and other non-water pixels within PS imagery, calculated as follows (Eq. 1):

$$NDWI = \frac{BAND_{green} - BAND_{nir}}{BAND_{green} + BAND_{nir}} \tag{1}$$

The relevant information regarding the NDWI is provided in the **Supplementary Information (SI)**. Further, we avoid the mountain shadows and find the lake locations within the image. For this, a global threshold of 0.1 was applied to NDWI to initially exclude non-water pixels, and then binary thresholding (Otsu 1979) was applied. Binary

thresholding (Otsu 1979) was additionally applied to the near-infrared top-of-atmosphere reflectance. The near-infrared channel is selected because its wavelengths are least reflected by clear water bodies relative to other features; hence, water pixels appear the darkest as the mountain shadows. Mountain shadows were removed by applying a threshold of 90 to the hillshade raster calculated from the DEM based on the sun’s azimuthal and altitude angles recorded at the time of image acquisition. Such a loose threshold was applied due to the coarse resolution of DEM and the resultant hillshade at 30m to avoid the removal of adjacent lake features, so the shadows are removed partially. Then, an intersection of the binary rasters from NDWI, NIR, and hillshade was converted to polygons, from which features below 1000m² in the area were excluded to further reduce the noise. Therefore, the lake polygons greater than 1000m² in the area were selected for the EBM method, while the remaining lakes were mapped manually. These steps yield lake locations by identifying the boundaries of their pure water pixels. The methodological workflow is shown in Fig. 2, and all the steps of the methodology are depicted in **Supplementary Fig. 1**.

After the identification of lake locations, all potential lake polygons selected and revised manually were buffered incrementally by one meter to ensure that for each individual polygon, the corresponding region from the raw NDWI additionally encompasses the land and mixed pixels surrounding pure water pixels. The buffer of the potential lake polygon grows outward iteratively until the following condition holds true (Eq. 2).

$$A_{initial} > (A_{buffered} - A_{initial}) + (A_{initial} \times 0.2) \tag{2}$$

Where $A_{initial}$, $A_{buffered}$ are the areas of each polygon before and after the buffer was applied, respectively. This incremental buffering technique is known as a dynamic buffer, which helps us to easily identify land and water pixels. The dynamic buffer forms a bimodal histogram of the NDWI values with two distinct peaks (water peak and land peak) for each individual lake. The pixels outside the two peaks of the histogram refer to the pure land and water pixels, and the pixels inside the peaks are partially inundated (Fig. 3). Then, for each individual lake, we created the water fraction map by estimating the water fraction of each pixel from the NDWI image. For this, we first determined the thresholds that precisely identify the 100% land and 100% water pixels (Olthof et al. 2015) using Eqs. 3 and 4, respectively:

$$L_{100} = H_{Lpeak} - C \times Prom_{Lpeak} \tag{3}$$

$$W_{100} = H_{Wpeak} - C \times Prom_{Wpeak} \tag{4}$$

Here, C is a constant, which depends upon bimodal distribution, and if the value of this constant changes (**Sup-**

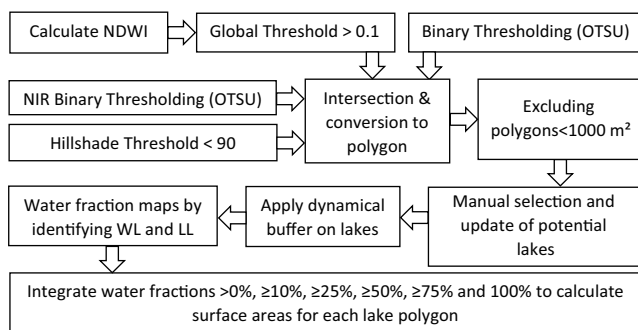


Fig. 2 Methodology workflow for lake mapping

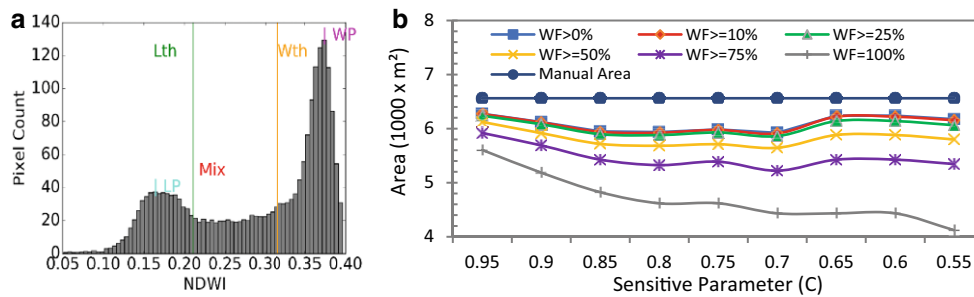


Fig. 3 The NDWI histogram of a buffered lake polygon (a). Note: Water and land peaks are labeled in magenta and cyan, and water (wth) and land (lth) thresholds are labeled in yellow and green, respectively. Mix indicates the region of mixed pixels. b are the lake areas mapped semi-automatically against each value of C, compared to the manually mapped reference lake area

plementary Fig. 2) the region of the histogram containing mixed pixels also varies in other words this parameter defines the limits of the mixed pixel region, whereas L_{100} and W_{100} are the thresholds for 100% land and 100% water pixels, H_{Lpeak} and H_{Wpeak} are the land and water peak heights within the histogram, and $Prom_{Lpeak}$ and $Prom_{Wpeak}$ are the prominences of the land and water peaks, respectively. The prominence of a peak refers to its significance due to its fundamental elevation and its position relative to other peaks. After determining the L_{100} and W_{100} , thresholds, water fractions (WF) for each NDWI pixel were calculated using Eq. 5:

$$WF = \frac{NDWI - L_{100}}{W_{100} - L_{100}} \quad (5)$$

Pixels with NDWI values $\geq W_{100}$ have a water fraction of one and are designated as pure (or 100%) water pixels, whereas pixels with NDWI values $\leq L_{100}$ were given a water fraction of zero and are designated as pure (or 100%) land pixels. The pixels between W_{100} and L_{100} were assigned their water fractions between zero and one. Once water fractions are estimated, the total area of each lake was calculated using Eq. 6:

$$Larea = \Sigma(WF \times Parea) \quad (6)$$

Where *Larea* is the total area of a lake and *Parea* is the area of an individual image pixel. We hypothesize that the inclusion of pixels featuring minute water fraction may not be necessary for PS imagery at a higher resolution of ~3 m, but important for the coarser-resolution imagery from Sentinel-2 and Landsat-8, etc. To check what water fractions are important to precisely estimate the lake area, we considered six different water fractions, i.e., >0%, $\geq 10\%$, $\geq 25\%$, $\geq 50\%$, $\geq 75\%$, and 100%.

2.3.4 Manual Mapping Uncertainty

The lakes were digitized manually for validation via visual inspection and interpretation. Glacial lake extraction from remote sensing imagery using manual visual delineation is often accompanied by errors related to image quality. The area error in glacial lake boundary extraction based on remote sensing images can be roughly ± 0.5 pixels. Because pure lake water body pixels are typically surrounded by mixed pixels, the theoretical maximum area error in glacial lake boundary extraction is half the area of the edge pixels. According to Hanshaw and Bookhagen (2014), the uncertainty in the lake area of a single glacial lake can be calculated as follows (Eqs. 7 and 8):

$$Error(1\sigma) = \frac{P}{G} \times \frac{G^2}{2} \times 0.6872 \quad (7)$$

$$Error_{relative}(\%) = \frac{Error(1\sigma)}{A} \times 100 \quad (8)$$

where *P* is the perimeter of the glacial lake (m), *G* is the spatial resolution of the PlanetScope imagery (3.125 m), 0.6872 is the 1 standard deviation (1σ), $Error_{relative}$ is the relative error, and *A* denotes the lake area (m^2).

2.3.5 Lake Volume and Depth Estimation

GLOF risk reduction and management entail information regarding the possibility and intensity of outburst events. For the GLOF risk assessment, a large lake volume indicates greater flooding potential in the case of an outburst event. However, flood volume also depends on other imperative factors, such as the trigger mechanisms, status, and characteristics of the lake and damming material (Emmer and Vilfemek 2014). Therefore, volume and depth analyses of lakes are essential. However, estimation of lake volume is challenging owing to the presence of these lakes in harsh and inaccessible environments, which prevents bathymet-

ric surveys of lake basins. At present, neither the information on the volume of glacial lakes nor their bathymetry is available within the Karakoram or Himalaya region of the Indus basin. This hinders the estimation of lake volumes or their changes, which are crucial for GLOF risk reduction and mitigation. Here, we estimate the lake volumes based on empirical area-volume relationships developed from the lake measurements given in **Supplementary Table 2**.

The estimation of lake depths based on empirical relationships is the best alternative when in-situ measurements are not available (Carrivick and Quincey 2014; Loriaux and Casassa 2013; Yao et al. 2012). However, caution must be practiced as the lake area and the mean depth do not always scale predictably (Cook and Quincey 2015). This is because glaciers experience a varying intensity of erosion, the height of moraine dams varies, shallow lakes form on stagnant ice (Yao et al. 2012), sediments could deposit into the lakes (Allen et al. 2009), and due to the existence of a lake outlet, etc. We have used the empirical relationships to estimate the mean depth of the mapped glacier lakes (**Supplementary Table 2**).

3 Results and Discussion

3.1 Sensitivity Analysis of Lake Mapping

We observed that precise lake area mapping is sensitive to the choice of select parameters of global NDWI threshold, hillshade threshold, and the value of C . For the global NDWI threshold, we tested different values to successfully identify lake locations from multiple NDWI images and visually inspected their results. We found that to correctly identify the location and shape of lake water pixels, the global threshold must vary depending on the image, the lake type, and its geometry, which hinders the automation of the mapping process. Against this background, we selected 0.1 as the safe global threshold irrespective of the image and the lake type because higher global thresholds may remove pure water pixels, and we only need to remove a majority of non-water pixels to input to the binary thresholding. The same procedure was followed for determining the hillshade threshold, and its value was fixed at 90.

For identifying the optimum value of C , the lake area estimated from the automated procedure was compared to the manually delineated lake for each value of C . The results are shown in Fig. 3 and are summarized in Table 1. We found that varying the value of C changes the thresholds that identify pure land and water pixels, markedly changing the resultant lake area (Table 2). We further assessed whether changes in the estimated lake area occurred due to varying C are compensated by the water fraction percentages considered for calculating the total lake area. We found that as

Table 1 Variation of water (wth) and land threshold (lth) for a given sensitive parameter (C)

Parameter (C)	NDWI (lth)	NDWI (wth)
0.95	0.196	0.261
0.90	0.196	0.276
0.85	0.196	0.291
0.80	0.191	0.296
0.75	0.186	0.296
0.70	0.186	0.301
0.65	0.156	0.301
0.60	0.156	0.301
0.55	0.156	0.306

the value of C decreases, the wth and lth thresholds become stricter and yield a smaller number of pure land and water pixels. Subsequently, the region of mixed pixels within the NDWI bimodal histogram expands with a greater number of mixed pixels, resulting in an overall underestimation of the observed lake area (**Supplementary Fig. 2**). Our results suggest that the optimum range for the sensitive parameter C is between 0.95 and 0.9, where $C=0.95$ yields the lake area closest to the observation. For identifying optimum water fractions, we note that as we decrease the value of C , integrating only higher water fraction pixels further underestimates the observed lake area. Such an underestimation is marked for water fractions higher than 25%. These findings imply that the integration of pixels with smaller water fractions becomes more important for precise area calculation when the number of mixed pixels is relatively large. This is particularly true for shallow lakes or their shallow shorelines. Hence, we have fixed the value of C to 0.95 for the rest of the analysis.

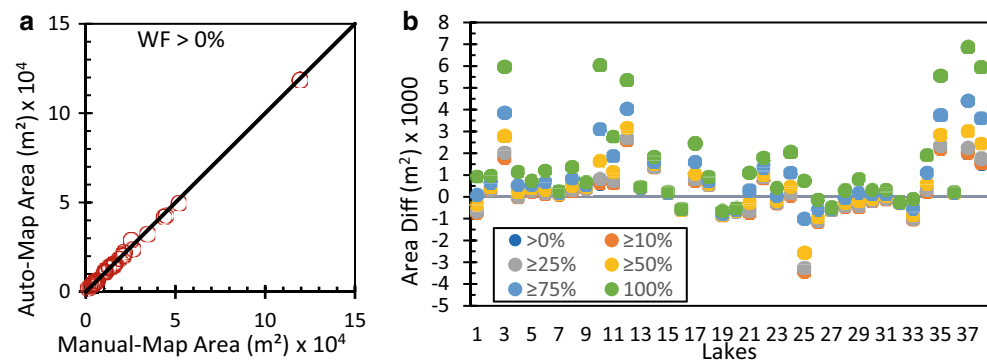
3.2 Validation Against Reference Datasets

Areas from the semi-automatedly delineated lakes using $C=0.95$ were compared with the 38 lakes manually delineated from the same cloud-free PS image of 01 September 2018 (Fig. 4). The comparison was performed on pixels inundated with any water fraction greater than zero. We found a minute bias of -0.71% , indicating that our lake areas slightly underestimate the reference lake areas. This bias is within the range of the uncertainty that is associated with the manual lake area mapping, which assumes an error of ± 0.5 pixel for at least one-third of the pixels along the shoreline (Fujita et al. 2009; Salerno et al. 2012). Our results suggest that as we integrate only higher water fractions, the underestimation becomes higher and approaches 9% of the reference dataset when only pixels featuring 100% water fractions are considered for area calculations (Table 3). Nonetheless, higher values of R^2 (>0.99), lower values of

Table 2 Variation of an example lake area according to water fraction for a given sensitive parameter (C). Note: Water fraction is the percentage of the pixel inundated in water

Sensitive parameter (C)	(wf>0%)	(wf≥10%)	(wf≥25%)	(wf≥50%)	(wf≥75%)	(wf=100%)
0.95	6275.25	6268.59	6238.61	6124.04	5919.03	5605.47
0.90	6120.25	6113.88	6081.26	5917.37	5689.65	5185.55
0.85	5947.68	5940.63	5897.26	5718.69	5425.87	4824.22
0.80	5936.08	5924.02	5880.42	5683.68	5323.85	4619.14
0.75	5985.20	5975.91	5927.71	5712.31	5387.45	4619.14
0.70	5921.62	5911.77	5861.85	5646.37	5221.00	4433.59
0.65	6239.96	6220.22	6139.91	5882.46	5425.22	4433.59
0.60	6239.96	6220.22	6139.91	5882.46	5425.22	4433.59
0.55	6174.43	6155.35	6063.33	5800.05	5343.63	4121.09

Fig. 4 Semi-automatically vs. manually delineated areas of 38 reference lakes from PS imagery dated 01 September 2018, **a** Areas calculated considering >0% (all) water fractions are shown, **b** Differences in areas considering certain water fractions for integration



PBIAS (−0.71%), and negligible RMSE and NRMSE suggest that the semi-automated lake area mapping approach is robust and can precisely map lakes of various sizes and complexities in mountainous terrain. Figure 5 shows spatial maps of six lakes with their shorelines, considering the pixels with different water fractions in addition to manually delineated shorelines. Considerable differences can be seen for either shallower lakes or their shallower shorelines, for which mixed pixels are higher in number relative to large lakes with deep shorelines. The comparison of the mean of all multiple automatic digitization of lake outlines with the manually mapped lake outlines is reported in **Supplementary Table 3**.

3.3 Validation Across Platforms

We assessed whether our methodology can precisely map glacial lakes on varying coarse resolution imagery from the Sentinel-2 and Landsat-8. For this, the areas of the 22 lakes mapped automatically from the PS, Sentinel-2,

and Landsat-8 images of similar dates were compared to the manually mapped areas using PS imagery. We assessed such across-platform robustness of our methodology (DBL) for similar breakpoint methods considering a single NDWI histogram based either on constant buffered lakes (CBI) or varying buffered lakes for the whole image (DBI). The results are shown in Fig. 6 and are summarized in Table 4.

Across-platform comparison using DBL methodology suggests that as the resolution becomes coarser, the lake areas are underestimated relative to 22 manually delineated lakes. Such an underestimation is negligible for the PS and Landsat-8 and around 2.38% for the Sentinel-2 imagery. However, the lake area estimates for the Sentinel-2 (10m) are closer to that of PS whereas marked underestimation for the Landsat-8 is due to its spatial resolution, which is ten times coarser than that of PS imagery. Overall, DBL yields relatively robust results for PS and Sentinel-2 owing to their high resolution relative to the Landsat-8 imagery. This indicates that resolution has a significant impact as far as precise lake area mapping is concerned. This also sug-

Table 3 RMSE, NRMSE, R², and PBias (%) of water fractionated area of lakes for C=0.95

Parameter	Lake Areas for Given Water Fractions					
	>0%	≥10%	≥25%	≥50%	≥75%	100%
RMSE	0.0010	0.0010	0.0011	0.0012	0.0016	0.0022
NRMSE	0.0619	0.0624	0.0644	0.0712	0.0922	0.1267
R ²	0.9988	0.9988	0.9987	0.9987	0.9985	0.9976
PBias (%)	−0.71	−0.78	−1.16	−2.53	−4.95	−8.96

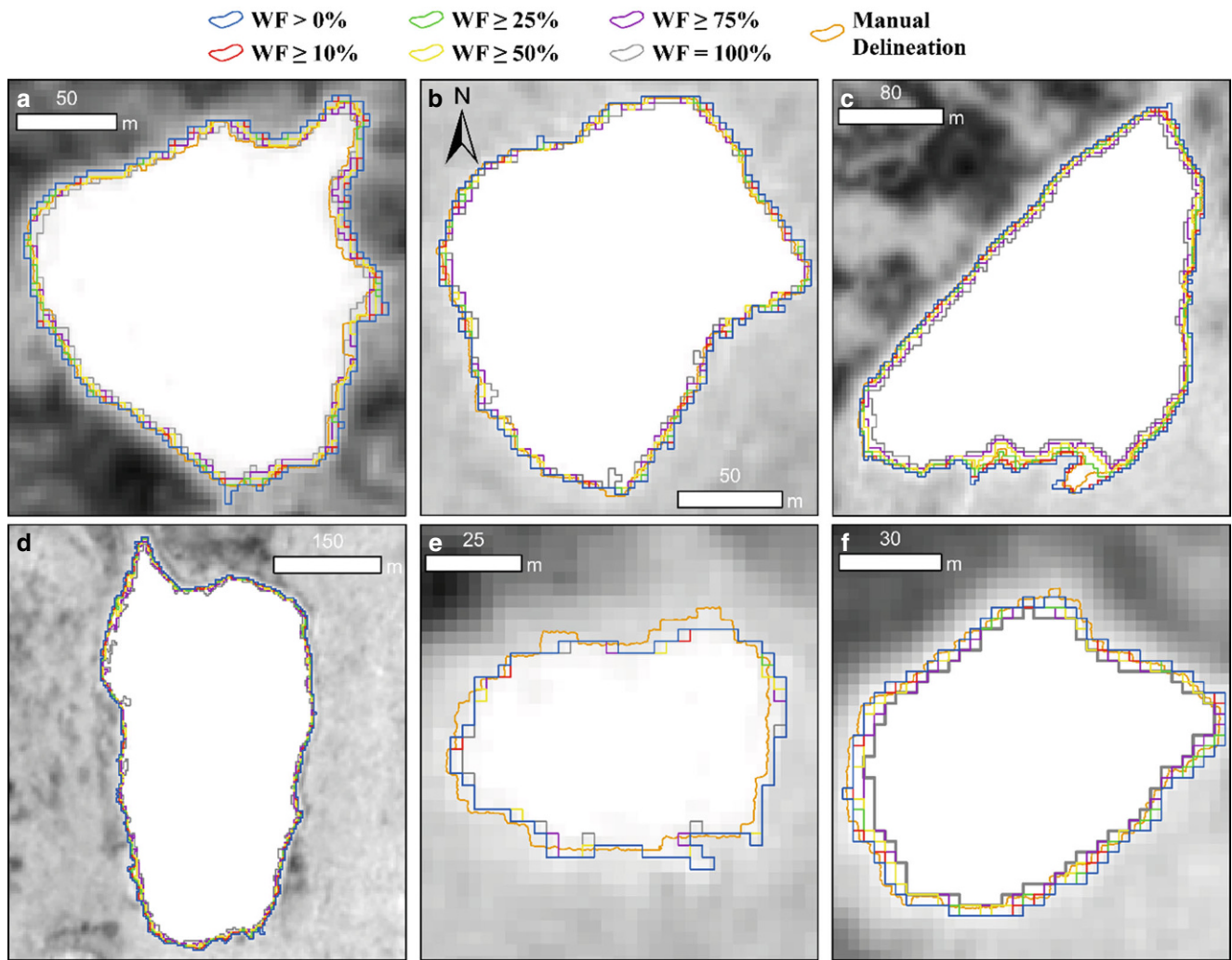
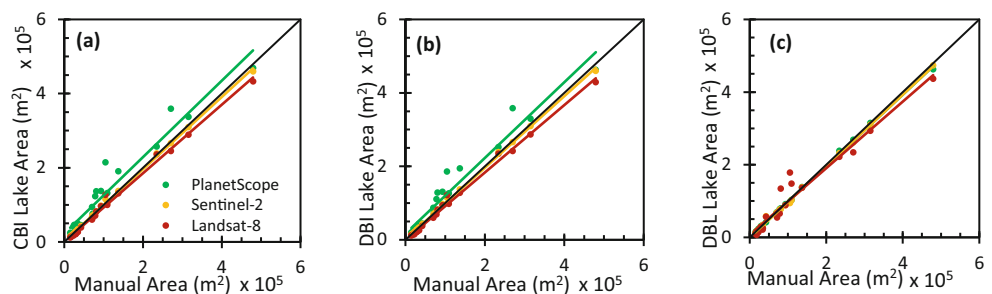


Fig. 5 Spatial maps of semi-automatically and manually delineated lake shorelines from PS imagery considering pixels of different water fractions

Fig. 6 Relationship between manually and semi-automatically delineated lake areas across platforms using methodologies of: **a** Constant Buffer on Image (CBI), **b** Dynamic Buffer on Image (DBI), and, **c** Dynamic Buffer on individual Lake (DBL)



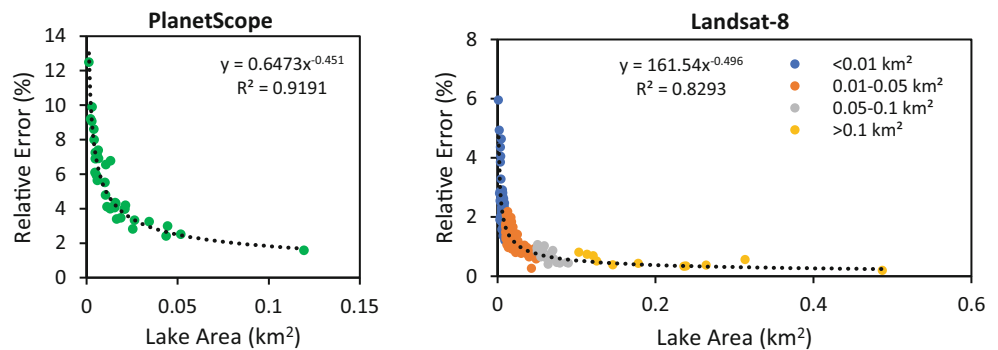
gests that the DBL method using high-resolution CubeSat imagery of PS allows the mapping of lake areas with high accuracy.

The DBI-based across-platform comparison exhibits an opposite response, suggesting an overestimation for the PS. The lake areas are close to the reference lake areas for the Sentinel-2 with a negligible negative mean bias, followed by an overestimation of 19% for the PS. The CBI methodol-

ogy likewise maps lake areas closer to reference lake areas for the Sentinel-2, followed by the Landsat-8 with around -7% underestimation. Surprisingly, CBI method substantially overestimates lake areas (>24%) for the PS imagery. It also yields the highest NRMSE for the PS relative to DBI and DBL. This confirms that the constant buffer for the glacial lakes is not an optimum choice for precise mapping of lake areas using high-resolution imagery.

Table 4 List of statistical parameters across methodology

Scenario	Description	Platform	R^2	RMSE	NRMSE (%)	PBias (%)
CBI	Constant Buffer Image	PlanetScope	0.94	0.039	36.9	24.72
CBI	Constant Buffer Image	Sentinel-2	0.99	0.005	5.1	-1.24
CBI	Constant Buffer Image	Landsat-8	0.99	0.014	13.8	-7.14
DBI	Dynamic Buffer Image	PlanetScope	0.95	0.033	31.4	19.07
DBI	Dynamic Buffer Image	Sentinel-2	0.99	0.005	5.0	-1.21
DBI	Dynamic Buffer Image	Landsat-8	0.99	0.015	14.7	-8.53
DBL	Dynamic Individual Lake	PlanetScope	0.99	0.004	4.19	-1.83
DBL	Dynamic Individual Lake	Sentinel-2	0.99	0.005	5.1	-2.38
DBL	Dynamic Individual Lake	Landsat-8	0.95	0.026	24.6	-1.54

Fig. 7 Relationship of relative area error vs. area of manually mapped glacial lakes

Overall, a comparison between methodologies across platforms suggests that the dynamic buffer around glacial lakes is necessary either areas are calculated from a single image-based or individual lake-based NDWI histogram. This means the CBI method should be avoided for mapping glacier lakes from high-resolution imagery. Besides the high resolution of PS imagery, its NRMSE is higher for both CBI and DBI. This shows that especially for PS imagery, CBI and DBI are the least preferred methods, and the precise lake areas can only be obtained by the DBL approach. The lowest RMSE and the highest R^2 for the DBL method for all platforms except Landsat-8 further suggest the same. Although DBI can yield better results for coarse-resolution imagery, the DBL method clearly outperforms DBI for high-resolution PS imagery.

3.4 Manual Mapping Uncertainty

We noted that as lake size increases, the relative error of individual glacial lakes decreases, as indicated by the uncertainty estimated from Eq. 8. Smaller lakes typically have higher relative errors. The estimated error for a large lake is less than for a small lake since the relative error was calculated as a function of lake perimeter and satellite image spatial resolution. The relative area errors of the manually mapped lakes varied from 1.56 to 12.48% and 0.19 to 5.95% via PlanetScope and Landsat-8, respectively (Fig. 7).

3.5 Lake Area Mapping

Lake inventories for the years 2018 and 2019 were mapped semi-automatically within Astore Basin using PS imagery based on the DBL method. We compared both inventories, and their changes are quantified. We also compared the 2018 lake inventory with the PMD inventory of 2013. We note that lakes are more densely distributed on the Southern and Eastern flanks and sparsely distributed on the Northern and Western flanks of the basin (Fig. 8).

A comparison between 2013 and 2018 inventories revealed a heterogeneous pattern of glacial lake evolution, such as incidences of disappearance, formation, shrinkage, and expansion (Fig. 8). Nine lakes drained were not present anymore until 2018, corresponding to a lake area loss of 0.064 km². On the other hand, around 135 glacial lakes emerged in 2018 relative to 2013, accounting for an area of 0.50 km². These newly mapped 135 glacial lakes from PlanetScope were either not present or not detected in 2013 due to the coarse resolution of the Landsat imagery and methodology difference. The reasons for the formation and development of glacial lakes depend upon glacier geomorphological characteristics, calving processes, subaqueous melting mechanisms, and ice-face ablation phenomena (Gardelle et al. 2011; Thompson et al. 2012). A comparison of 2018 and 2019 lake inventories revealed that ten lakes drained were not present anymore until 2019, corresponding to a lake area loss of 0.041 km². In contrast, around ten

Fig. 8 Lake Area changes between **a** 2013–2018 and **b** 2018–2019. The lake area increase is shown in blue and the decrease in red. Note: Black circles indicate vanished lakes, while yellow circles show newly mapped lakes

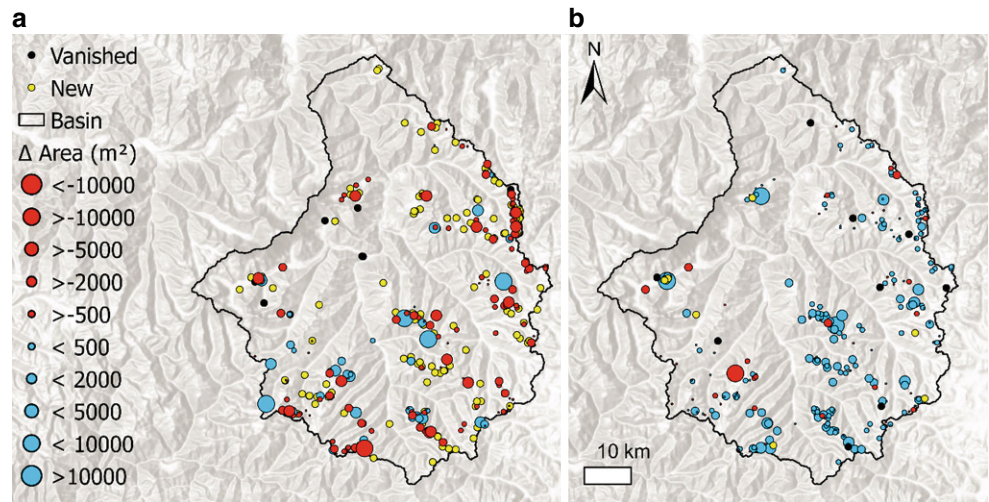
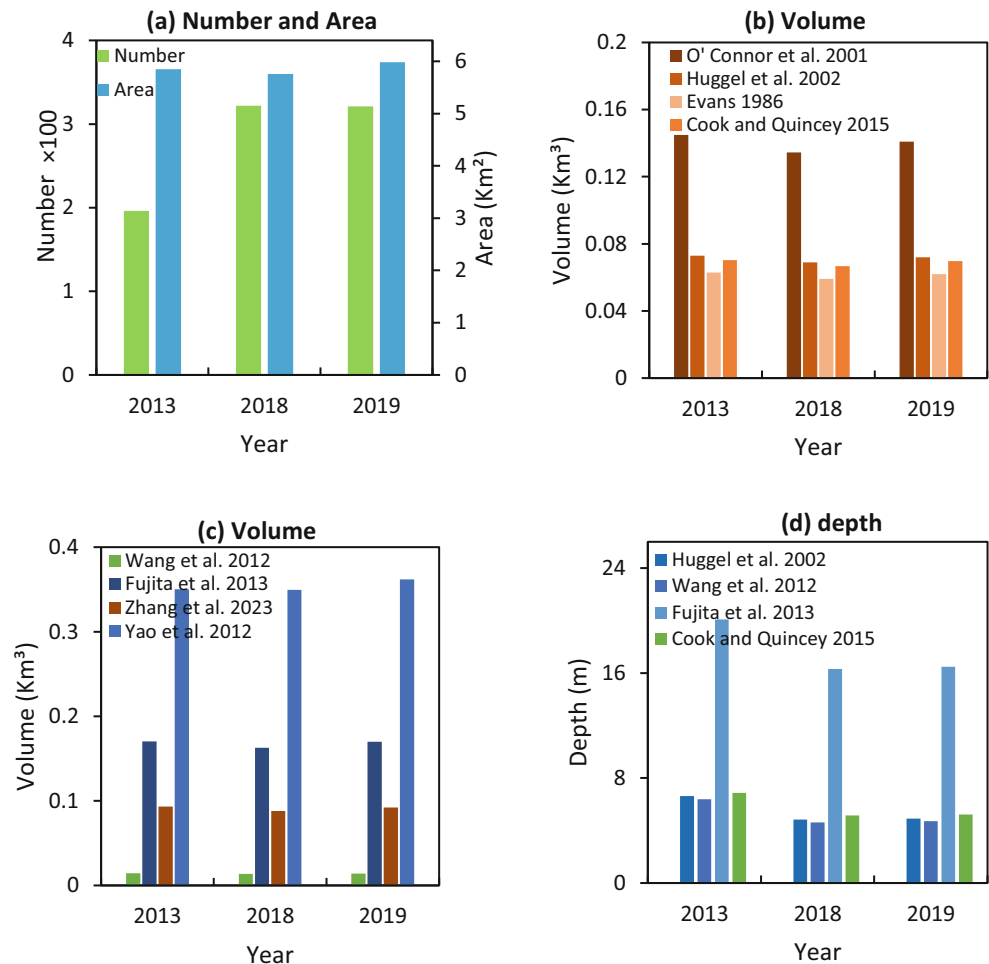


Fig. 9 **a** Total number and area of lakes Overall, **b** estimated volume of lakes using empirical methods based on regions outside the Himalayas, **c** estimated volume of lakes using the empirical relationships within the Himalayas, and **d** mean depths of lakes



glacial lakes emerged in 2019 relative to 2018, accounting for an area of 0.016km². Between 2018 and 2019, the total number of lakes almost remained the same.

The total number of lakes and the sum of their corresponding areas were determined, as shown in Fig. 9a. In 2013, 196 lakes, corresponding to a total area of 5.847 km²,

were identified in the Astore Basin. In 2018 and 2019, 322 and 321 lakes were mapped with a total area of 5.759 and 5.980km², respectively. Between 2013 and 2018, 40 lakes experienced an expansion, whereas 147 lakes have seen a shrinkage in their areas. Between 2018 and 2019, 213 lakes expanded, whereas 98 lakes shrank. A sub-

stantial area increase has been observed for four lakes (0.012–0.042 km²) between 2013 and 2018 and for three lakes (0.014–0.025 km²) between 2018 and 2019. These extensively expanded lakes could further be assessed for additional criteria to designate them as potentially dangerous for GLOF. Besides the loss of nine lakes in 2018 relative to 2013 and ten lakes in 2019 relative to 2018 and several lakes shrinking since 2013, the total lake area within the Astore basin has increased by 2019. The expansion of glacial lakes is strongly associated with broader and more extensive valleys and smoother topography, which provides an appropriate setting for lake development (Song et al. 2016).

Owing to marked variation, the glacial lake areas were classified based on their sizes into four categories, such as >0.1, 0.05–0.1, 0.01–0.05, and <0.01 km², as shown in **Supplementary Fig. 4**. In 2013, most lakes were of the category 0.01–0.05 km², which corresponds to 91 lakes out of 196 total lakes (46.43%) with an area of 1.905 km² (32.58%). On the other hand, very few lakes belonged to the largest category >0.1 km² with only 11 lakes (5.61%) covering the total area of 2.329 km² (39.83%). In 2018 and 2019, most lakes were present in the category of <0.01 km², with 206 (63.97%) and 203 (63.24%) lakes corresponding to a total area of 0.716 km² (12.43%) and 0.721 km² (12.06%), respectively. For both 2018 and 2019, only 10 lakes were present in the category of >0.1 km²

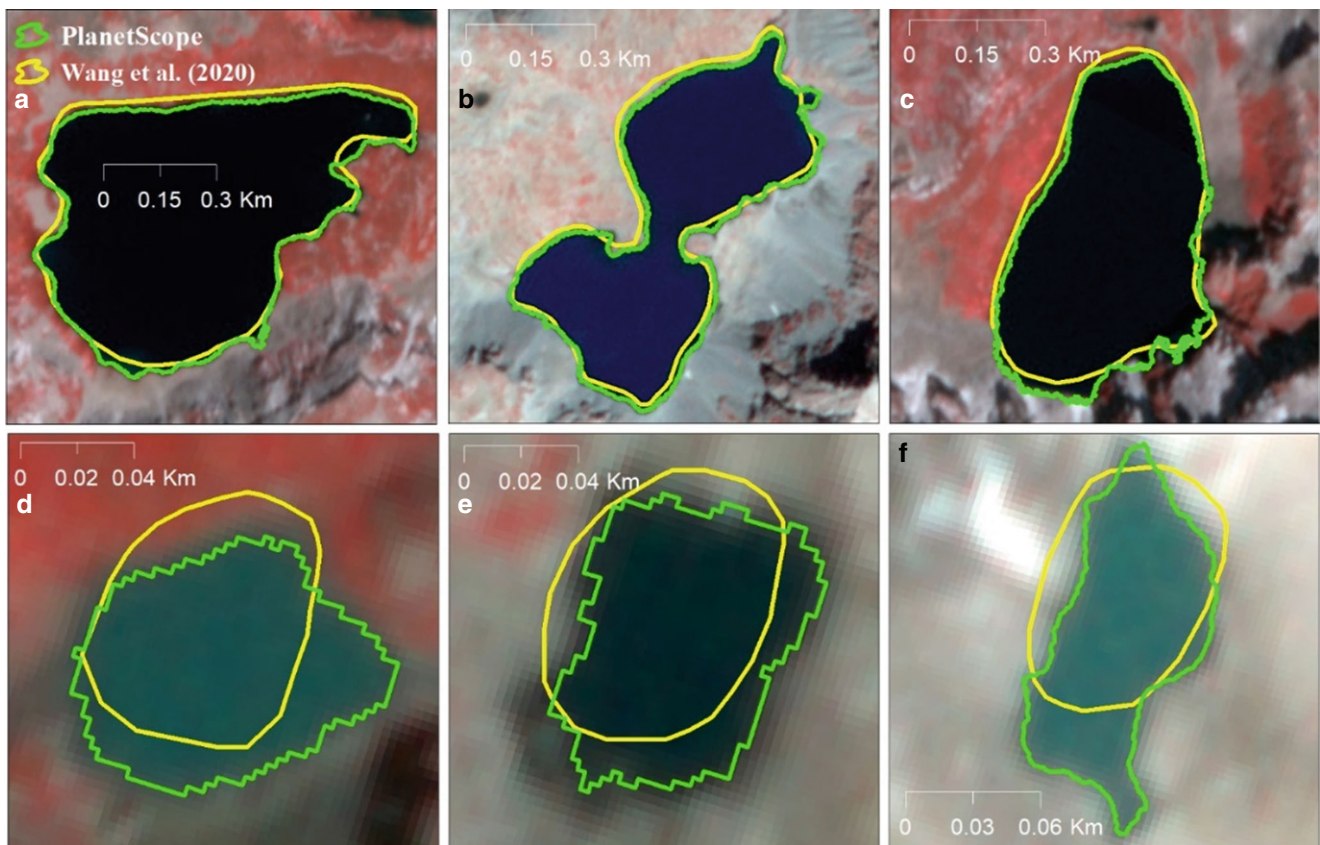


Fig. 10 Comparison of semi-automatically delineated lake shoreline using PS (green) with those delineated by Wang et al. (2020) using Landsat images (yellow) for the year 2018

Table 5 Differences of 2018 PS inventory with Wang et al. (2020)

Lake No.	Area (m ²) Wang et al. (2020)	Area (m ²) PlanetScope	Absolute Difference (m ²)	Absolute Difference (%)
1	480,609	456,203	24,406	5.35
2	264,787	255,054	9733	3.82
3	247,688	236,496	11,192	4.73
4	5562	6275	713	11.36
5	6159	5781	378	6.54
6	6840	7435	595	8.00

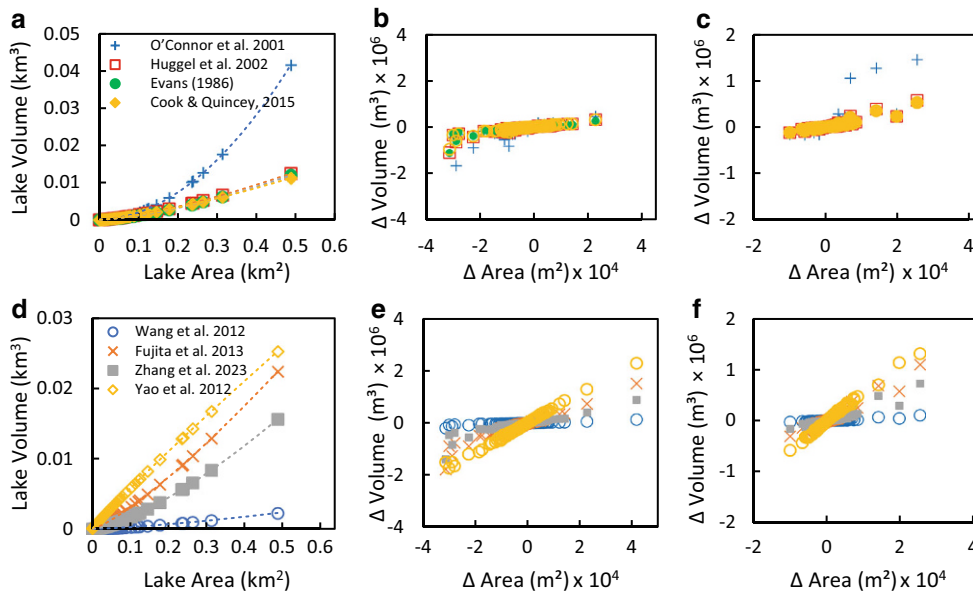


Fig. 11 **a** Area vs. volume relationship in 2013 using empirical methods based on regions outside the Himalayas, **b** Change in volume vs change in area for 2018 relative to 2013 using empirical methods based on regions outside the Himalayas, **c** Change in volume vs Change in area for 2019 relative to 2018 using empirical methods based on regions outside the Himalayas, **d** Area vs. volume relationship in 2013 using empirical methods based on regions within the Himalayas, **e** Change in volume vs change in area for 2018 relative to 2013 using empirical methods based on regions within the Himalayas, **f** Change in volume vs Change in the area for 2019 relative to 2018 using empirical methods based on regions within the Himalayas

(3.10% for 2018 and 3.11% for 2019), featuring a total area of 2.109 km² (36.62%) and 2.167 km² (36.24%) in 2018 and 2019, respectively. Overall, we found most of the lakes in the Astore Basin to be smaller than <0.05 km².

We compared the PS-based inventory of 2018 with the regional inventory from Wang et al. (2020), prepared using the Landsat images of 2018. In Fig. 10, the first row depicts the three best cases of large lakes where the regional inventory successfully delineates, however, its performance is poor for the smaller and shallower lakes as shown in three cases in the second row. The lake sizes can be noted from the map scale shown for each lake, and their corresponding areas are shown in Table 5. This problem could be explained by the lack of local precision in the regional lake inventories, which ignore the local details and delicate problems associated with the lakes. Wang et al. (2020) mapped 106 lakes in total with an area of 4.57 km² within the Astore basin. In comparison to PS inventory, Wang et al. (2020) underestimate areas for 29 lakes, and overestimate areas for 77 lakes. Overall, Wang et al. (2020) overestimate the 2018 lakes by 5.61% for the Astore basin. These findings suggest that the regional inventory estimates may represent large-scale features or their qualitative changes; however, relying on their estimates on a local scale is not adequate. This further emphasizes developing the local scale inventories using very high-resolution satellite imagery.

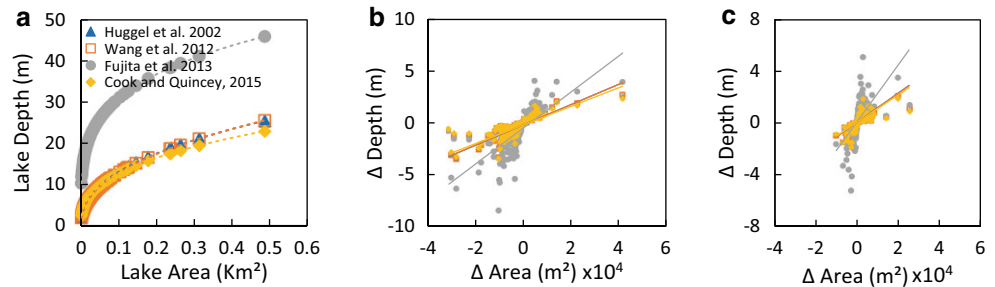
3.6 Lake Volume and Depth Estimation

The area and volume relationship of glacial lakes delineated in 2013, 2018, and 2019 was determined using the empirical relationships, as shown in Fig. 11. It is evident from the results that the volume estimated using the empirical relationships of Huggel et al. (2002), Evans (1986), and Cook and Quincey (2015) are close to each other, as compared to those proposed by O’Connor et al. (2001). The volumes estimated via the area-volume relationships proposed by

Table 6 Summary of the total lake volumes in 2013, 2018, and 2019 estimated via empirical relationships

Empirical Relationship	2013 (Volume km ³)	2018 (Volume km ³)	2019 (Volume km ³)
O’Connor et al. (2001)	0.145	0.134	0.141
Huggel et al. (2002)	0.073	0.069	0.072
Evans (1986)	0.063	0.059	0.062
Cook and Quincey (2015)	0.070	0.067	0.069
Wang et al. (2012)	0.014	0.013	0.014
Fujita et al. (2013)	0.170	0.162	0.169
Zhang et al. (2023)	0.093	0.088	0.092
Yao et al. (2012)	0.350	0.349	0.362

Fig. 12 a Lake area-depth relationship in 2013 as proposed by Huggel et al. (2002), Wang et al. (2012), Fujita et al. (2013), Cook and Quincey, (2015) b difference in area and depths for the 2013–2018 period, c difference in area and depth for 2018–2019



Wang et al. (2012), Fujita et al. (2013), Zhang et al. (2023), and Yao et al. (2012) vary depending on the empirical relationship used. These area-volume relationships generally suggest that as the area increases, the lake volume also increases (Fig. 11a, d).

The total volume of lakes in 2013, 2018, and 2019 estimated using empirical relationships are summarized in Table 6. Although the number of lakes substantially increased in 2018 and 2019 relative to 2013, the areas of individual lakes were relatively smaller, leading to approximately the same volume in 2013 and 2019. A comparison of volume between inventories is shown in (Fig. 9b, c). Although we could not validate these estimates against in-situ measurements, we weighed the method of Huggel et al. (2002) more than other methods because several studies in the HKH region have used this relationship to estimate the volume of glacial lakes (Singh et al. 2023; Rashid et al. 2020; Khan et al. 2021; Muneeb et al. 2021; Sarwar and Mahmood 2024; Siddique and Rahman 2023).

Between 2013 and 2018, 40 lakes saw a positive volume change of 0.0025 km^3 (20.57%), whereas 147 lakes experienced a negative change of 0.0088 km^3 (14.59%). Between 2018 and 2019, 213 lakes have gained volume by 0.0044 km^3 (9.11%), whereas 98 lakes have lost their volume by 0.0010 km^3 (5.09%). The distribution of lake volumes was also analyzed based on the area size classes (Supplementary Fig. 4). This analysis revealed that bigger lakes present in the category of $>0.1 \text{ km}^2$ have more volume and the smaller lakes present in the category of $<0.01 \text{ km}^2$ have less volume in all three years. Although the bigger lakes are less in number, their volume is more owing to their large areas.

Table 7 Summary of the mean lake depths in 2013, 2018, and 2019 estimated via empirical relationships

Empirical Relationship	2013 (Depth m)	2018 (Depth m)	2019 (Depth m)
Huggel et al. (2002)	6.63	4.83	4.91
Wang et al. (2012)	6.39	4.62	4.71
Fujita et al. (2013)	20.09	16.31	16.47
Cook and Quincey (2015)	6.88	5.15	5.23

Moreover, the depth of the lakes was also estimated by using the empirical relationships summarized in Table 7. In 2013, 2018, and 2019, the mean depth of the lakes was 6.6, 4.8, and 4.9 m, respectively, according to the empirical relationship of Huggel et al. (2002), as shown in Fig. 9d. These area-depth relationships mostly suggest that as the lake area grows, the lake depth also increases (Fig. 12a). The mean depths estimated via the empirical relationships of Huggel et al. (2002), Wang et al. (2012), and Cook and Quincey (2015) are closer to each other relative to the empirical relationship of Fujita et al. (2013). According to area sizes, the lakes present in the area categories of $0.05\text{--}0.1$ and $>0.1 \text{ km}^2$ feature the maximum mean depth, whereas lakes lying in the small area categories of $0.01\text{--}0.05$ and $<0.01 \text{ km}^2$ are the shallowest (Supplementary Fig. 4). Since lakes with a depth $>10 \text{ m}$ may cause substantial outburst events (Furian et al. 2021), we determined 25, 24, and 25 lakes passed that threshold in 2013, 2018, and 2019, respectively, according to the empirical relationship of Huggel et al. (2002). This emphasizes further investigation of these lakes for additional criteria to designate them as potentially dangerous.

3.7 Limitations of the Study and the Implications of the Findings

As part of Planet Labs' research and education program, we obtained a 4-band top-of-atmosphere reflectance product with a 3.125 m resolution free of cost. A semi-automated delineation approach was used to prepare an inventory of the glacial lakes. Although this automatic classification method can speed up the detection of glacial lakes, it cannot be applied to the entire region owing to uncertainties created by atmospheric and physical processes. For example, if lakes are fully or partially frozen or covered with snow, or obstructed by cloud cover, they cannot be detected using this automatic classification method. Further, mountain shadows present in the satellite imagery can be mapped as lakes due to their closer spectral similarity (Fig. 13). In such cases, manual post-processing is required.

Shadow removal is a major concern when mapping the glacial lakes within the mountainous region using optical imagery because their spectral signatures are similar

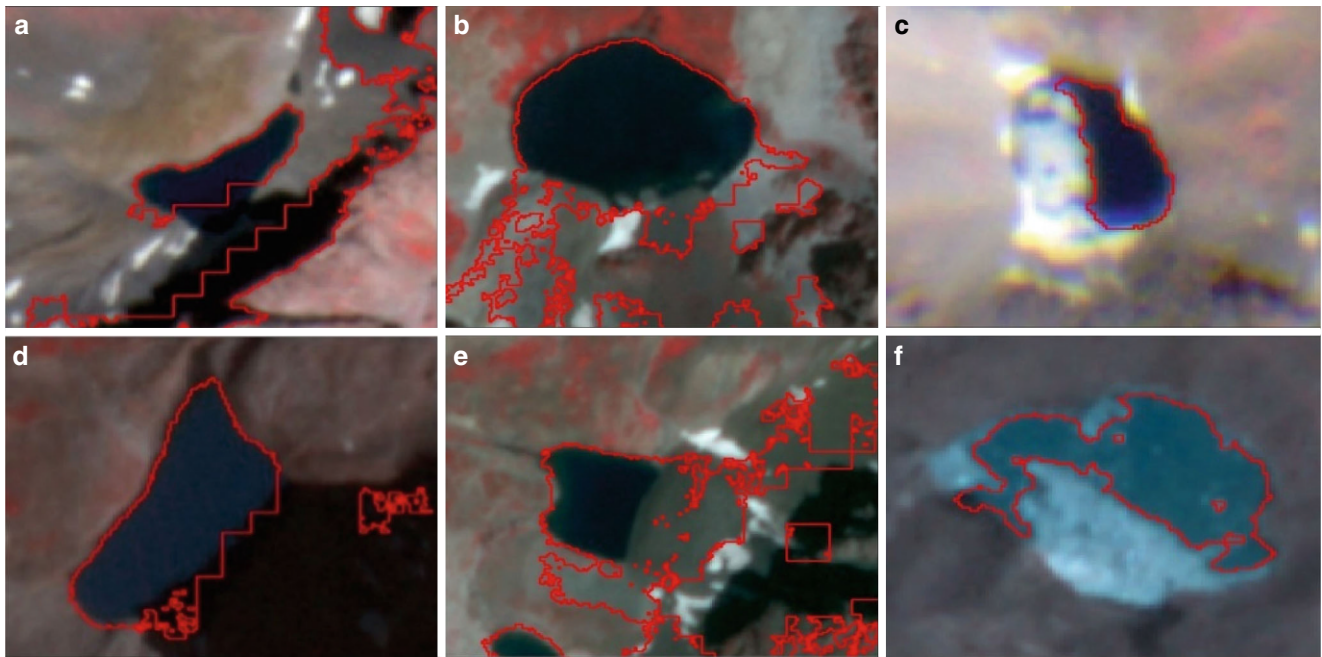


Fig. 13 a, d lakes with shadows, b, e lakes with highly saturated soil, c, f frozen lakes

to glacial lakes with low turbidity (Gardelle et al. 2011). Therefore, shadowed areas can be misclassified as potential lake polygons and require attention (Li and Sheng 2012; Salvador et al. 2001; Su et al. 2016). One strategy to delineate such lakes is to increase the hillshade threshold, which then requires high-resolution DEM not available for our study. This strategy works to some extent because the dynamic buffer can again include shadow pixels; hence, a bimodal histogram cannot be obtained.

Snow removal was also problematic to some extent because of the band limitation in first and second-generation PS imagery from the Dove Classic and Dover-R flocks. Water surfaces can easily be distinguished from non-water surfaces using Green and NIR bands. For ice and snow discrimination from liquid water, a combination of NIR and mid-infrared (MIR) bands is required, which is not possible due to the absence of MIR in PS. Furthermore, the short-wave infrared (SWIR) band is crucial for improved water classification compared to the NIR band (Du et al. 2014; Ji et al. 2009; Li et al. 2013). However, PS observes a narrow range of electromagnetic spectra, ranging from 455 to 860 nm. Hence, MIR and SWIR are not available, limiting the ability to differentiate between clouds, open water, ice, and snow (Hall et al. 2002). Furthermore, frozen lakes covered by snow cannot be classified using a semi-automated method because of the different responses to frozen and liquid water. Lakes in contact with glaciers were also difficult to delineate due to their similar responses; thus, the shape of the potential lake polygon was disturbed. These problems at present lead to some manual postprocessing.

The performance of water indices regarding glacial lake mapping is reliable under consistent spectral conditions, but at the same time, care must be taken while implementing such techniques because water spectrally resembles mountain and cloud shadows (Su et al. 2016). Hence, glacial lake mapping accuracy is compromised to some extent while using optical remote sensing datasets, owing to the presence of frequent clouds and steep mountainous slopes in glacierized regions. These issues can be tackled by using Synthetic Aperture Radar (SAR) datasets such as Sentinel-1 (Zhang et al. 2019) and Radarsat-2 (Strozzi et al. 2012).

In conclusion, the automated lake delineation approach can be challenging for the mapping of turbid lakes, lakes partially covered by snow and ice, and lakes present in shadow zones. The development of advanced mapping techniques using machine or deep learning may solve these problems (Wangchuk and Bolch 2020).

The estimation of lake volume and depth is indispensable for disaster risk assessment and management. Therefore, the study employed empirical relationships to estimate the volume and depth of the lakes. Since we are unable to conduct detailed bathymetric surveys due to the region's inaccessible terrain and severe weather conditions, we have to rely on empirical relationships. We caution the reader to take these estimates carefully, and we need to emphasize the bathymetric surveys, which are beyond the scope of this study.

There are some limitations to relying upon the empirical relationships for lake depth and volume estimation. For example, region-specific datasets are used to derive the

empirical relationships. These relationships might produce erroneous findings if applied to lakes in different geographical locations. The accuracy of these relationships relies upon the quality of the initial data that was utilized to construct them. The biases in the training datasets may appear in the derived relationships. These relationships overlook vital aspects by oversimplifying the complex physical processes that affect lake morphometry. Therefore, we suggest field-based bathymetric surveys for better accuracy in future studies.

In light of the unprecedented climate change, it is imperative to continuously monitor the glacial lakes and their vulnerability to outburst floods. To ensure the well-being and protection of the communities living in the downstream vulnerable areas, long-term planning and adaptation strategies are vital. The concerned authorities and policymakers can more efficiently and effectively formulate management plans to reduce the impacts of outburst floods on susceptible communities by comprehending the dynamics of the PDGLs.

4 Conclusions

In this study, we propose an enhanced breakpoint method (EBM) that determines the thresholds for pure water pixels and surrounding land pixels for each lake based on an individual NDWI bimodal histogram prepared by applying a varying or a dynamical buffer around the lake polygon. The EBM can resolve the issue of local precision owing to the treatment of each lake as a unique object.

Our results suggest that a semi-automated EBM outperforms similar methods and precisely maps glacial lakes of all sizes and complexities with little manual editing using high-resolution imagery from PlanetScope as well as coarser resolution imagery from Sentinel-2 and Landsat-8 platforms. We found that the lake areas estimated via PS and Sentinel-2 are close to each other due to their high resolution, while the lake areas estimated using Landsat-8 imagery were underestimated owing to its coarse resolution.

Glacial lake inventories (2018 and 2019) mapped in this study provide valuable information about the current state of the lakes in terms of area, volume, and depth. These glacial lake inventories revealed that the Astore Basin is home to a considerable number of lakes of variable sizes. Intercomparison of 2018 and 2019 inventories and the existing 2013 inventory revealed heterogeneous lake formations, disappearances, expansions, and shrinkage patterns. Some new lakes were formed, and the previously present lakes disappeared. Overall, the number and area of lakes significantly increased, and changes observed for 2018–2019 are higher than that of the 2013–2018 period.

The EBM using daily PlanetScope imagery at ~3 m allows precise monitoring of lake evolutions with low latency time to reduce and mitigate outburst flooding risks in complex terrain. In the future, there is a potential to develop a web tool for monitoring dynamic lakes along with GLOF early warning systems. Frequent mapping and continuous monitoring will aid in GLOF risk reduction. Moreover, an automated methodology will reduce the labor-intensive and time-consuming process of glacial lake mapping. The approach discussed in this study would provide grounds for planning and managing GLOF-related hazards.

Supplementary Information The online version of this article (<https://doi.org/10.1007/s41064-025-00345-y>) contains supplementary material, which is available to authorized users.

Acknowledgements The authors wish to express their gratitude to Planet Labs Inc. and USGS for data provision which helped complete our joint effort. The authors acknowledge the support from the Deutsche Forschungsgemeinschaft (DFG, German Research Foundation) under Germany's Excellence Strategy- EXC 2037 "CLICCS-Climatic Change, and Society"-Project Number: 390683824, contribution to the Center for Earth System Research and Sustainability (CEN) of Universität Hamburg. The authors also acknowledge the funding from the DFG-funded project "Sensitivity and Response of Treeline Ecotones in the Nepal Himalaya to Climate Warming - TREELINE-II" (DFG, BO 1333/4-1). S.u. Hasson also acknowledges the support from the German Academic Exchange Service (DAAD, Project ID 57609231) for the initial duration 2022-23, and subsequent DAAD Project (ID#57708475) for 2024.

Author Contribution Conceptualization: Mustafa Javed, Jürgen Böhner, Shabeh ul Hasson; Methodology: Mustafa Javed, Jürgen Böhner, Shabeh ul Hasson; Formal analysis and investigation: Mustafa Javed; Writing—original draft preparation: Mustafa Javed; Writing—review and editing: Jürgen Böhner, Shabeh ul Hasson; Supervision: Jürgen Böhner, Shabeh ul Hasson

Funding Open Access funding enabled and organized by Projekt DEAL.

Conflict of interest M. Javed, J. Böhner and S.u. Hasson declare that they have no competing interests.

Open Access This article is licensed under a Creative Commons Attribution 4.0 International License, which permits use, sharing, adaptation, distribution and reproduction in any medium or format, as long as you give appropriate credit to the original author(s) and the source, provide a link to the Creative Commons licence, and indicate if changes were made. The images or other third party material in this article are included in the article's Creative Commons licence, unless indicated otherwise in a credit line to the material. If material is not included in the article's Creative Commons licence and your intended use is not permitted by statutory regulation or exceeds the permitted use, you will need to obtain permission directly from the copyright holder. To view a copy of this licence, visit <http://creativecommons.org/licenses/by/4.0/>.

References

- Adrian R, O'Reilly CM, Zagarese H, Baines SB, Hessen DO, Keller W, Livingstone DM, Sommaruga R, Straile D, Van Donk E et al (2009) Lakes as sentinels of climate change. *Limnol Oceanogr*

- 54(6part2):2283–2297. https://doi.org/10.4319/lo.2009.54.6_part_2.2283
- Ahmad I, Ahmad Z, Munir S, Shah SRA, Shabbir Y et al (2018) Geospatial dynamics of snow cover and hydro-meteorological parameters of Astore basin, UIB, HKH Region, Pakistan. *Arab J Geosci* 11(15):419. <https://doi.org/10.1007/s12517-018-3734-9>
- Ahmed R, Ahmad ST, Wani GF, Mir RA, Ahmed P, Jain SK (2022) High-resolution inventory and hazard assessment of potentially dangerous glacial lakes in upper Jhelum basin, Kashmir Himalaya, India. *Geocarto Int* 37(25):10681–10712. <https://doi.org/10.1080/10106049.2022.2038693>
- Ali G, Hasson S, Khan AM (2009) Climate change: implications and adaptation of water resources in Pakistan. Global Change Impact Studies Centre (GCISC), Islamabad
- Allen S, Schneider D, Owens IF (2009) First approaches towards modelling glacial hazards in the Mount Cook region of New Zealand's Southern Alps. *Nat Hazards Earth Syst Sci* 9:481–499. <https://doi.org/10.5194/nhess-9-481-2009>
- Bajracharya SR, Mool P (2009) Glaciers, glacial lakes, and glacial lake outburst floods in the Mount Everest region, Nepal. *Ann Glaciol* 50(53):81–86. <https://doi.org/10.3189/172756410790595895>
- Bhambri R, Misra A, Kumar A, Gupta AK, Verma A, Tiwari SK (2018) Glacier lake inventory of Himachal Pradesh. *Himal Geol* 39(1):1–32
- Bolch T, Shea JM, Liu S, Azam FM, Gao Y, Gruber S, Zhang Y (2019) Status and change of the cryosphere in the extended Hindu Kush Himalaya region. In: *The Hindu Kush Himalaya assessment: mountains, climate change, sustainability and people*, pp 209–255 https://doi.org/10.1007/978-3-319-92288-1_7
- Carrivick JL, Quincey DJ (2014) Progressive increase in number and volume of ice-marginal lakes on the western margin of the Greenland ice sheet. *Glob Planet Change* 116:156–163. <https://doi.org/10.1016/j.gloplacha.2014.02.009>
- Chen F, Zhang M, Guo H, Allen S, Kargel JS, Haritashya UK, Watson CS (2020) Annual 30-meter dataset for glacial lakes in high mountain Asia from 2008 to 2017. *Earth Syst Sci Data Discuss.* <https://doi.org/10.5194/essd-13-741-2021>
- Cook SJ, Quincey DJ (2015) Estimating the volume of Alpine glacial lakes. *Earth Surf Dyn Discuss.* <https://doi.org/10.5194/esurf-3-559-2015>
- Cooley SW, Smith LC, Stepan L, Mascaro J (2017) Tracking dynamic northern surface water changes with high-frequency planet CubeSat imagery. *Remote Sens* 9(12):1306. <https://doi.org/10.3390/rs9121306>
- Das S, Das S, Mandal ST, Sharma MC, Ramsankaran R (2024) Inventory and GLOF susceptibility of glacial lakes in Chenab basin, Western Himalaya. *Geomatics Nat Hazards Risk.* <https://doi.org/10.1080/19475705.2024.2356216>
- Dietz AJ, Klein I, Gessner U, Frey CM, Kuenzer C, Dech S (2017) Detection of water bodies from AVHRR data—A TIMELINE thematic processor. *Remote Sens* 9(1):57. <https://doi.org/10.3390/rs9010057>
- Ding Y, Mu C, Wu T, Hu G, Zou D, Wang D, Li W, Wu X (2021) Increasing cryospheric hazards in a warming climate. *Earth Sci Rev* 213:103500. <https://doi.org/10.1016/j.earscirev.2020.103500>
- Du Z, Li W, Zhou D, Tian L, Ling F, Wang H, Gui Y, Sun B (2014) Analysis of landsat-8 OLI imagery for land surface water mapping. *Remote Sens Lett* 5(7):672–681. <https://doi.org/10.1080/2150704X.2014.960606>
- Emmer A, Vilimek V (2014) New method for assessing the potential hazardousness of glacial lakes in the Cordillera Blanca, Peru. *Hydrol Earth Syst Sci* 18:346–13479. <https://doi.org/10.5194/hess-18-3461-2014>
- Evans SG (1986) Landslide damming in the Cordillera of Western Canada. *Landslide dams: processes, risk, and mitigation*, pp 111–130
- Fujita K, Sakai A, Nuimura T, Yamaguchi S, Sharma RR (2009) Recent changes in Imja glacial lake and its damming moraine in the Nepal Himalaya revealed by in situ surveys and multi-temporal ASTER imagery. *Environ Res Lett* 4(4):45205. <https://doi.org/10.1088/1748-9326/4/4/045205>
- Fujita K, Sakai A, Takenaka S, Nuimura T, Surazakov AB, Sawagaki T, Yamanokuchi T (2013) Potential flood volume of Himalayan glacial lakes. *Nat Hazards Earth Syst Sci* 13(7):1827–1839. <https://doi.org/10.5194/nhess-13-1827-2013>
- Furian W, Loibl D, Schneider C (2021) Future glacial lakes in high mountain Asia: an inventory and assessment of hazard potential from surrounding slopes. *J Glaciol* 67(264):653–670. <https://doi.org/10.1017/jog.2021.18>
- Gardelle J, Arnaud Y, Berthier E (2011) Contrasted evolution of glacial lakes along the Hindu Kush Himalaya mountain range between 1990 and 2009. *Glob Planet Change* 75(1–2):47–55. <https://doi.org/10.1016/j.gloplacha.2010.10.003>
- Gupta A, Maheshwari RS, Guru N, Rao BS, Raju PV, Rao VV (2022) Updated glacial lake inventory of Indus river basin based on high-resolution Indian remote sensing satellite data. *J Indian Soc Remote Sens.* <https://doi.org/10.1007/s12524-021-01452-0>
- Hall DK, Riggs GA, Salomonson VV, DiGirolamo NE, Bayr KJ (2002) MODIS snow-cover products. *Remote Sens Environ* 83(1–2):181–194. [https://doi.org/10.1016/S0034-4257\(02\)00095-0](https://doi.org/10.1016/S0034-4257(02)00095-0)
- Hanshaw MN, Bookhagen B (2014) Glacial areas, lake areas, and snow lines from 1975 to 2012: status of the Cordillera Vilcanota, including the Quelccaya ice cap, Northern Central Andes, Peru. *Cryosphere* 8(2):359–376. <https://doi.org/10.5194/tc-8-359-2014>
- Harrison S, Kargel JS, Huggel C, Reynolds J, Shugar DH, Betts RA, Emmer A, Glasser N, Haritashya UK, Klimeš J, Reinhardt L, Schaub Y, Wiltshire A, Regmi D, Vilimek V (2018) Climate change and the global pattern of moraine-dammed glacial lake outburst floods. *Cryosphere* 12(4):1195–1209. <https://doi.org/10.5194/tc-12-1195-2018>
- Hasson S (2016) Seasonality of precipitation over Himalayan watersheds in CORDEX South Asia and their driving CMIP5 experiments. *Atmosphere* 7(10):123. <https://doi.org/10.3390/atmos7100123>
- Hasson S, Lucarini V, Khan MR, Petitta M, Bolch T, Gioli G (2014) Early 21st century snow cover state over the Western river basins of the Indus river system. *Hydrol Earth Syst Sci* 18(10):4077–4100. <https://doi.org/10.5194/hess-18-4077-2014>
- Hasson S, Böhner J, Lucarini V (2017) Prevailing climatic trends and runoff response from Hindukush-Karakoram-Himalaya, upper Indus basin. *Earth Syst Dyn* 8(2):337–355. <https://doi.org/10.5194/esd-8-337-2017>
- Hayat H, Akbar TA, Tahir AA, Hassan QK, Dewan A, Irshad M (2019) Simulating current and future river-flows in the Karakoram and Himalayan regions of Pakistan using snowmelt-runoff model and RCP scenarios. *Water* 11(4):761. <https://doi.org/10.3390/w11040761>
- Hock R, Rasul G, Adler C, Cáceres B, Gruber S, Hirabayashi Y, Zhang Y (2019) High mountain areas. In: Pörtner H-O, Roberts DC, Masson-Delmotte V, Zhai P, Tignor M, Poloczanska E, Mintenbeck K, Alegría A, Nicolai M, Okem A, Petzold J, Rama B, Weyer NM (eds) *The IPCC special report on the ocean and cryosphere in a changing climate*, pp 131–202 <https://doi.org/10.1017/9781009157964.004>
- Huggel C, Käib A, Haerberli W, Teyssie P, Paul F (2002) Remote sensing based assessment of hazards from glacier lake outbursts: a case study in the Swiss Alps. *Can Geotech J* 39(2):316–330. <https://doi.org/10.1139/t01-099>
- Ives JD, Shrestha RB, Mool PK (2010) Formation of glacial lakes in the Hindu Kush-Himalayas and GLOF risk assessment. *ICIMOD, Kathmandu*

- Ji L, Wylie B, Rover J (2008) Estimating percent surface-water area using intermediate resolution satellite imagery. AGU fall meeting abstracts, vol 2008, pp H41B–874
- Ji L, Zhang L, Wylie B (2009) Analysis of dynamic thresholds for the normalized difference water index. *Photogramm Eng Remote Sensing* 75(11):1307–1317. <https://doi.org/10.14358/PERS.75.11.1307>
- Khadka N, Zhang G, Thakuri S (2018) Glacial lakes in the Nepal Himalaya: inventory and decadal dynamics (1977–2017). *Remote Sens* 10(12):1913. <https://doi.org/10.3390/rs10121913>
- Khan G, Ali S, Xiangke X, Qureshi JA, Ali M, Karim I (2021) Expansion of Shishper glacier lake and recent glacier lake outburst flood (GLOF), Gilgit-Baltistan, Pakistan. *Environ Sci Pollut Res* 28:20290–20298. <https://doi.org/10.1007/s11356-020-11929-z>
- Klein I, Dietz AJ, Gessner U, Galayeva A, Myrzakhmetov A, Kuenzer C (2014) Evaluation of seasonal water body extents in Central Asia over the past 27 years derived from medium-resolution remote sensing data. *Int J Appl Earth Obs Geoinf* 26:335–349. <https://doi.org/10.1016/j.jag.2013.08.004>
- Li J, Sheng Y (2012) An automated scheme for glacial lake dynamics mapping using landsat imagery and digital elevation models: a case study in the Himalayas. *Int J Remote Sens* 33(16):5194–5213. <https://doi.org/10.1080/01431161.2012.657370>
- Li J, Sheng Y, Luo J (2011) Automatic extraction of Himalayan glacial lakes with remote sensing. *Yaogan Xuebao J Remote Sens* 15(1):29–43
- Li W, Du Z, Ling F, Zhou D, Wang H, Gui Y, Sun B, Zhang X (2013) A comparison of land surface water mapping using the normalized difference water index from TM, ETM+ and ALI. *Remote Sens* 5(11):5530–5549. <https://doi.org/10.3390/rs5115530>
- Li W, Wang W, Gao X, Wang X, Wang R (2022) Inventory and spatiotemporal patterns of glacial lakes in the HKH-TMHA region from 1990 to 2020. *Remote Sens* 14(6):1351. <https://doi.org/10.3390/rs14061351>
- Loriaux T, Casassa G (2013) Evolution of glacial lakes from the Northern Patagonia Icefield and terrestrial water storage in a sea-level rise context. *Glob Planet Change* 102:33–40. <https://doi.org/10.1016/j.gloplacha.2012.12.012>
- Mal S, Kumar A, Bhambri R, Schickhoff U, Singh RB (2020) Inventory and spatial distribution of glacial lakes in Arunachal Pradesh, Eastern Himalaya, India. *J Geol Soc India* 96:609–615. <https://doi.org/10.1007/s12594-020-1610-1>
- McFeeters SK (1996) The use of the Normalized Difference Water Index (NDWI) in the delineation of open water features. *Int J Remote Sens* 17(7):1425–1432. <https://doi.org/10.1080/01431169608948714>
- Miehe G, ul Hasson S, Glaser B, Mischke S, Böhner J, van der Knaap WO, Habertzettl T (2021) Föhn, fire and grazing in Southern Tibet? A 20,000-year multi-proxy record in an alpine ecotonal ecosystem. *Quat Sci Rev* 256:106817. <https://doi.org/10.1016/j.quascirev.2021.106817>
- Muneeb F, Baig SU, Khan JA, Khokhar MF (2021) Inventory and GLOF susceptibility of glacial lakes in Hunza river basin, Western Karakorum. *Remote Sens* 13(9):1794. <https://doi.org/10.3390/rs13091794>
- Nie Y, Sheng Y, Liu Q, Liu L, Liu S, Zhang Y, Song C (2017) A regional-scale assessment of Himalayan glacial lake changes using satellite observations from 1990 to 2015. *Remote Sens Environ* 189:1–13. <https://doi.org/10.1016/j.rse.2016.11.008>
- Nie Y, Liu Q, Wang J, Zhang Y, Sheng Y, Liu S (2018) An inventory of historical glacial lake outburst floods in the Himalayas based on remote sensing observations and geomorphological analysis. *Geomorphology* 308:91–106. <https://doi.org/10.1016/j.geomorph.2018.02.002>
- O'Connor JE, Hardison JH, Costa JE (2001) Debris flows from failures of neoglacial-age moraine dams in the Three Sisters and Mount Jefferson wilderness areas vol 1606. US Department of the Interior, US Geological Survey, Oregon <https://doi.org/10.3133/pp1606>
- Olthof I, Fraser RH, Schmitt C (2015) Landsat-based mapping of thermokarst lake dynamics on the Tuktoyaktuk coastal plain, Northwest Territories, Canada since 1985. *Remote Sens Environ* 168:194–204. <https://doi.org/10.1016/j.rse.2015.07.001>
- Otsu N (1979) A threshold selection method from gray-level histograms. *IEEE Trans Syst, Man, Cybern* 9(1):62–66. <https://doi.org/10.1109/TSMC.1979.4310076>
- Pepin N, Bradley RS, Diaz HF, Baraer M, Caceres EB, Forsythe N, Fowler H, Greenwood G, Hashmi MZ, Liu XD, Miller JR, Ning L, Ohmura A, Palazzi E, Rangwala I, Schöner W, Severskiy I, Shahgedanova M, Wang MB, Mountain Research Initiative EDW Working Group (2015) Elevation-dependent warming in mountain regions of the world. *Nat Clim Chang* 5(5):424–430. <https://doi.org/10.1038/nclimate2563>
- Plug LJ, Walls C, Scott BM (2008) Tundra lake changes from 1978 to 2001 on the Tuktoyaktuk peninsula, Western Canadian Arctic. *Geophys Res Lett*. <https://doi.org/10.1029/2007GL032303>
- Rashid I, Majeed U, Jan A, Glasser NF (2020) The January 2018 to September 2019 surge of Shisper glacier, Pakistan, detected from remote sensing observations. *Geomorphology* 351:106957. <https://doi.org/10.1016/j.geomorph.2019.106957>
- Roach JK, Griffith B, Verbyla D (2012) Comparison of three methods for long-term monitoring of boreal lake area using Landsat TM and ETM+ imagery. *Can J Remote Sens* 38(4):427–440
- Rover J, Wylie BK, Ji L (2010) A self-trained classification technique for producing 30 m percent-water maps from landsat data. *Int J Remote Sens* 31(8):2197–2203. <https://doi.org/10.1080/01431161003667455>
- Salerno F, Thakuri S, D'Agata C, Smiraglia C, Manfredi EC, Viviano G, Tartari G (2012) Glacial lake distribution in the Mount Everest region: uncertainty of measurement and conditions of formation. *Glob Planet Change* 92:30–39. <https://doi.org/10.1016/j.gloplacha.2012.04.001>
- Salvador E, Cavallaro A, Ebrahimi T (2001) Shadow identification and classification using invariant color models. 2001. IEEE International Conference on Acoustics, Speech, and Signal Processing. Proceedings, vol 01CH37221, pp 1545–1548 <https://doi.org/10.1109/ICASSP.2001.941227>
- Sarwar M, Mahmood S (2024) Exploring potential glacial lakes using geo-spatial techniques in Eastern Hindu Kush Region, Pakistan. *Nat Hazards Res* 4(1):56–61. <https://doi.org/10.1016/j.nhres.2023.07.003>
- Shrestha F, Gao X, Khanal NR, Maharjan SB, Shrestha RB, Wu L, Mool PK, Bajracharya SR (2017) Decadal glacial lake changes in the Koshi basin, central Himalaya, from 1977 to 2010, derived from landsat satellite images. *J Mt Sci* 14(10):1969–1984. <https://doi.org/10.1007/s11629-016-4230-x>
- Shugar DH, Burr A, Haritashya UK, Kargel JS, Watson CS, Kennedy MC, Bevington AR, Betts RA, Harrison S, Strattman K (2020) Rapid worldwide growth of glacial lakes since 1990. *Nat Clim Chang* 10(10):939–945. <https://doi.org/10.1038/s41558-020-0855-4>
- Siddique F, Rahman AU (2023) Genesis and spatio-temporal analysis of glacial lakes in the peri-glacial environment of Western Himalayas. *Int J Eng Geosci* 8(2):154–164. <https://doi.org/10.26833/ijeg.1097912>
- Singh H, Varade D, de Vries MVW, Adhikari K, Rawat M, Awasthi S, Rawat D (2023) Assessment of potential present and future glacial lake outburst flood hazard in the Hunza valley: a case study of Shisper and Mochowar glacier. *Sci Total Environ* 868:161717. <https://doi.org/10.1016/j.scitotenv.2023.161717>

- Song C, Sheng Y, Ke L, Nie Y, Wang J (2016) Glacial lake evolution in the southeastern Tibetan plateau and the cause of rapid expansion of proglacial lakes linked to glacial-hydrogeomorphic processes. *J Hydrol Reg Stud* 540:504–514. <https://doi.org/10.1016/j.jhydrol.2016.06.054>
- Strozzi T, Wiesmann A, Kääb A, Joshi S, Mool P (2012) Glacial lake mapping with very high resolution satellite SAR data. *Nat Hazard Earth Syst Sci* 12(8):2487–2498. <https://doi.org/10.5194/nhess-12-2487-2012>
- Su N, Zhang Y, Tian S, Yan Y, Miao X (2016) Shadow detection and removal for occluded object information recovery in urban high-resolution panchromatic satellite images. *IEEE J Sel Top Appl Earth Obs Remote Sens* 9(6):2568–2582. <https://doi.org/10.1109/JSTARS.2016.2570234>
- Sun D, Yu Y, Goldberg MD (2011) Deriving water fraction and flood maps from MODIS images using a decision tree approach. *IEEE J Sel Top Appl Earth Observations Remote Sensing* 4(4):814–825. <https://doi.org/10.1109/JSTARS.2011.2125778>
- Tahir AA, Adamowski JF, Chevallier P, Haq AU, Terzago S (2016) Comparative assessment of spatiotemporal snow cover changes and hydrological behavior of the Gilgit, Astore and Hunza River basins (Hindukush-Karakoram-Himalaya region, Pakistan). *Meteorol Atmos Phys* 128(6):793–811. <https://doi.org/10.1007/s00703-016-0440-6>
- Thompson SS, Benn DI, Dennis K, Luckman A (2012) A rapidly growing moraine-dammed glacial lake on Ngozumpa Glacier, Nepal. *Geomorphology* 145:1–11. <https://doi.org/10.1016/j.geomorph.2011.08.015>
- Veh G, Korup O, Roessner S, Walz A (2018) Detecting Himalayan glacial lake outburst floods from landsat time series. *Remote Sens Environ* 207:84–97. <https://doi.org/10.1016/j.rse.2017.12.025>
- Veh G, Korup O, von Specht S, Roessner S, Walz A (2019) Unchanged frequency of moraine-dammed glacial lake outburst floods in the Himalaya. *Nat Clim Chang* 9(5):379–383. <https://doi.org/10.1038/s41558-019-0437-5>
- Verpoorter C, Kutser T, Seekell DA, Tranvik LJ (2014) A global inventory of lakes based on high-resolution satellite imagery. *Geophys Res Lett* 41(18):6396–6402. <https://doi.org/10.1002/2014GL060641>
- Wang X, Liu S, Ding Y, Guo W, Jiang Z, Lin J, Han Y (2012) An approach for estimating the breach probabilities of moraine-dammed lakes in the Chinese Himalayas using remote-sensing data. *Nat Hazard Earth Syst Sci* 12(10):3109–3122. <https://doi.org/10.5194/nhess-12-3109-2012>
- Wang X, Siegert F, Zhou A, Franke J (2013) Glacier and glacial lake changes and their relationship in the context of climate change, Central Tibetan plateau 1972–2010. *Glob Planet Change* 111:246–257. <https://doi.org/10.1016/j.gloplacha.2013.09.011>
- Wang X, Guo X, Yang C, Liu Q, Wei J, Zhang Y, Liu S, Zhang Y, Jiang Z, Tang Z (2020) Glacial lake inventory of high-mountain Asia in 1990 and 2018 derived from landsat images. *Earth Syst Sci Data* 12(3):2169–2182. <https://doi.org/10.5194/essd-12-2169-2020>
- Wangchuk S, Bolch T (2020) Mapping of glacial lakes using sentinel-1 and sentinel-2 data and a random forest classifier: strengths and challenges. *Sci Remote Sens* 2:100008. <https://doi.org/10.1016/j.srs.2020.100008>
- Weiss DJ, Crabtree RL (2011) Percent surface water estimation from MODIS BRDF 16-day image composites. *Remote Sens Environ* 115(8):2035–2046. <https://doi.org/10.1016/j.rse.2011.04.005>
- Worni R, Huggel C, Stoffel M (2013) Glacial lakes in the Indian Himalayas—From an area-wide glacial lake inventory to on-site and modeling based risk assessment of critical glacial lakes. *Sci Total Environ* 468–469:71–84. <https://doi.org/10.1016/j.scitotenv.2012.11.043>
- Yao F, Livneh B, Rajagopalan B, Wang J, Crétaux JF, Wada Y, Berge-Nguyen M (2023) Satellites reveal widespread decline in global lake water storage. *Science* 380(6646):743–749. <https://doi.org/10.1126/science.abo2812>
- Yao T, Xue Y, Chen D, Chen F, Thompson L, Cui P, Koike T, Lau WK-M, Lettenmaier D, Mosbrugger V et al (2019) Recent third pole’s rapid warming accompanies cryospheric melt and water cycle intensification and interactions between monsoon and environment: Multidisciplinary approach with observations, modeling, and analysis. *Bull Am Meteorol Soc* 100(3):423–444. <https://doi.org/10.1175/BAMS-D-17-0057.1>
- Yao X, Liu S, Sun M, Wei J, Guo W (2012) Volume calculation and analysis of the changes in moraine-dammed lakes in the North Himalaya: a case study of Longbasaba lake. *J Glaciol* 58(210):753–760. <https://doi.org/10.3189/2012JoG11J048>
- Yao XJ, Liu SY, Sun MP, Zhang XJ (2014) Study on the glacial lake outburst flood events in Tibet since the 20th century. *Ziran Ziyuan Xuebao* 29:1377–1390. <https://doi.org/10.11849/zrzyxb.2014.08.010>
- Zhang G, Yao T, Xie H, Wang W, Yang W (2015) An inventory of glacial lakes in the Third Pole region and their changes in response to global warming. *Glob Planet Change* 131:148–157. <https://doi.org/10.1016/j.gloplacha.2015.05.013>
- Zhang G, Bolch T, Yao T, Rounce DR, Chen W, Veh G, Wang W (2023) Underestimated mass loss from lake-terminating glaciers in the Greater Himalaya. *Nat Geosci* 16(4):333–338. <https://doi.org/10.1038/s41561-023-01150-1>
- Zhang M, Chen F, Tian B, Liang D (2019) Using a phase-congruency-based detector for glacial lake segmentation in high-temporal resolution sentinel-1a/1b data. *IEEE J Sel Top Appl Earth Observations Remote Sensing* 12(8):2771–2780. <https://doi.org/10.1109/JSTARS.2019.2900442>
- Zhang M, Chen F, Zhao H, Wang J, Wang N (2021) Recent changes of glacial lakes in the high mountain Asia and its potential controlling factors analysis. *Remote Sens* 13(18):3757. <https://doi.org/10.3390/rs13183757>
- Zhang T, Wang W, Gao T, An B, Yao T (2022) An integrative method for identifying potentially dangerous glacial lakes in the Himalayas. *Sci Total Environ* 806:150442. <https://doi.org/10.1016/j.scitotenv.2021.150442>
- Zhao H, Chen F, Zhang M (2018) A systematic extraction approach for mapping glacial lakes in high mountain regions of Asia. *IEEE J Sel Top Appl Earth Observations Remote Sensing* 11(8):2788–2799. <https://doi.org/10.1109/JSTARS.2018.2846551>
- Zheng G, Bao A, Allen S, Ballesteros-Cánovas JA, Yuan Y, Jiapaer G, Stoffel M (2021a) Numerous unreported glacial lake outburst floods in the Third Pole revealed by high-resolution satellite data and geomorphological evidence. *Sci Bull* 66:1270–1273. <https://doi.org/10.1016/j.scib.2021.01.014>
- Zheng G, Allen SK, Bao A, Ballesteros-Cánovas JA, Huss M, Zhang G, Stoffel M (2021b) Increasing risk of glacial lake outburst floods from future Third Pole deglaciation. *Nat Clim Chang* 11(5):411–417. <https://doi.org/10.1038/s41558-021-01028-3>